Dendritic domain-specific sampling of long-range axons shapes feedforward and feedback connectivity of L5 neurons — Source link ↗

Alessandro R. Galloni, Alessandro R. Galloni, Zhiwen Ye, Ede A. Rancz

Institutions: University College London, Francis Crick Institute

Related papers:

- The dendritic density field of a cortical pyramidal cell.

- Spatiotemporal functional organization of excitatory synaptic inputs onto macaque V1 neurons.

- Rethinking single neuron electrical compartmentalization: dendritic contributions to network computation in vivo.

- Comprehensive imaging of synaptic activity reveals dendritic growth rules that cluster inputs

- Mapping Function Onto Neuronal Morphology

1 # Dendritic domain-specific sampling of long-range axons shapes

2 # feedforward and feedback connectivity of L5 neurons

3

4 Alessandro R. Galloni[1,2], Zhiwen Ye[1] and Ede Rancz[1*]

5 [1]The Francis Crick Institute, London, United Kingdom; [2]University College London, United Kingdom.

6 *For correspondence: ede.rancz@crick.ac.uk

7

8

9 # Abstract

10 Feedforward and feedback pathways interact in specific dendritic domains to enable cognitive functions

11 such as predictive processing and learning. Based on axonal projections, hierarchically lower areas are

12 thought to form synapses primarily on dendrites in middle cortical layers, while higher-order areas are

13 posited to target dendrites in layer 1 and in deep layers. However, the extent to which functional

14 synapses form in regions of axo-dendritic overlap has not been extensively studied. Here, we use viral

15 tracing in the secondary visual cortex of mice to map brain-wide inputs to thick-tufted layer 5 pyramidal

16 neurons. Furthermore, we provide a comprehensive map of input locations through subcellular

17 optogenetic circuit mapping. We show that input pathways target distinct dendritic domains with far

18 greater specificity than appears from their axonal branching, often deviating substantially from the

19 canonical patterns. Common assumptions regarding the dendrite-level interaction of feedforward and

20 feedback inputs may thus need revisiting.

Introduction

One of the key organizing principles of connectivity within the neocortex is thought to be hierarchy between cortical areas. This notion was originally proposed by Hubel & Wiesel (Hubel & Wiesel 1962) to account for the increasing receptive field complexity in areas progressively further from the retina. In purely feedforward (FF) networks, such as artificial neural networks used successfully in computer vision (LeCun et al 2015), hierarchy is generally defined by synaptic distance from the sensory periphery. However, in highly recurrent networks like the cortex, it is not possible to apply this definition consistently beyond the initial levels. Instead, the laminar patterns of axonal projections are often used to deduce relative levels of hierarchy. For example, the projection from primary to secondary visual cortex, which is classically defined as FF, is characterised by dense axon terminations in middle cortical layers (particularly L4). Meanwhile, the projection from secondary to primary visual cortex, used as the basis for defining feedback (FB), primarily targets L1 and to a lesser extent deeper layers (Rockland & Pandya 1979). This pattern of FF and FB projections also appears in many other brain regions, and has been used as a proxy to describe the hierarchical relationships between a large number of areas across the brain (D'Souza et al 2016, D'Souza et al 2020, Felleman & Van Essen 1991, Harris et al 2019, Wang et al 2020b, Zeng 2018).

Projections, however, do not guarantee functional connections. The link between the two is called Peters' rule, which postulates that the probability of synaptic connections can be predicted from the overlap between axonal and dendritic arbours (Rees et al 2017). While overlap between axons and dendrites is necessary for synapses to form, it is far from sufficient. The link between axo-dendritic overlap and connection probability may thus be overly simplistic and requires further scrutiny. While some studies have found support for Peters' rule at the level of functional synaptic connectivity for interneurons (Fino & Yuste 2011, Packer et al 2013, Rieubland et al 2014), its general applicability has been refuted, at least for local networks, by dense anatomical reconstructions of retinal (Briggman et al 2011, Helmstaedter et al 2013, Kim et al 2014, Krishnaswamy et al 2015) and cortical circuits (Kasthuri et al 2015, Lee et al 2016). To investigate how this principle applies to long-range projections, a technique that has become widely adopted is subcellular channelrhodopsin-assisted circuit mapping (sCRACM). Here optogenetics is combined with spatially targeted optical stimulation to map the distribution of synaptic currents for a given input (Petreanu et al 2009). While this has been used to show that different presynaptic populations target dendritic subdomains with high specificity (Anastasiades et al 2021, Collins et al 2018, Hooks et al 2013, Yamawaki et al 2019), the extent to which this can be explained and predicted by the distribution of axons and dendrites remains largely an open question.

Whether axons target specific dendritic domains is a particularly important question in the case of layer 5 pyramidal neurons (L5PN), given their central role in several theories of cortical computation (Aru et al 2020, Guerguiev et al 2017, Larkum 2013, Richards et al 2019). For example, the interaction between FF and FB information streams across cortical layers (Larkum et al 2018) is thought to underlie sensory

57   perception (Larkum 2013, Takahashi et al 2020, Takahashi et al 2016) and implement global inference

58   algorithms such as predictive coding (Shipp 2016). These theories all rely heavily on the assumption that

59   FF connections target primarily basal dendrites while FB connections preferentially synapse onto the

60   apical tuft, and would need to be revised should this not be true. This assumption in turn rests on Peter's

61   rule, but the evidence for this remains circumstantial and a direct examination of Peters' rule across

62   multiple input pathways to individual neurons remains to be done.

63   Here we present a comprehensive description of the functional input connectivity to thick-tufted layer 5

64   (ttL5) pyramidal neurons in medial secondary visual cortex. In particular, we set out to answer three

65   questions: determine the source of input connectivity to ttL5 neurons using monosynaptically restricted

66   rabies tracing (Kim et al 2015, Reardon et al 2016), create a census of subcellular input maps using

67   sCRACM, and test Peters' rule directly by comparing synaptic input maps to the respective axonal

68   projection maps.

69

Results

71   To ensure recording from a homogeneous neuronal population, we used the Colgalt2-Cre mouse line

72   which specifically labels subcortically projecting, thick-tufted layer 5 (ttL5) neurons (Groh et al 2010, Kim

73   et al 2015). We focused our study on the medial secondary visual cortex (V2M) as higher order cortical

74   regions are likely to receive a broader diversity of long-range inputs than primary sensory cortices. V2M is

75   defined in the Mouse Brain In Stereotaxic Coordinates atlas (Franklin & Paxinos 2007) which can be used

76   to guide viral injections. Furthermore, as this atlas is based on cytoarchitecture, thus V2M can be visually

77   distinguished and selectively targeted in slice recordings, as has previously been done (Galloni et al

78   2020, Young et al 2021). For whole-brain rabies tracing, on the other hand, we adopted the more recently

79   developed Allen Common Coordinate Framework (CCFv3, (Wang et al 2020a). This atlas allowed us to

80   localize individual neurons within 3D volumes of brain tissue, which is not possible using the Franklin &

81   Paxinos atlas. Within the CCFv3, area V2M corresponds to VISpm, VISam, and RSPagl (Lyamzin &

82   Benucci 2019), all of which are known to be visually responsive (Garrett et al 2014, Powell et al 2020).

83   Treating V2M as a single area for this study was also supported by the observation that axonal

84   projections to VISpm, VISam, and RSPagl are not substantially different (Figure S1, see Methods for

85   details).

Brain-wide input map to V2M ttL5 pyramidal neurons

87   We employed a monosynaptically restricted rabies virus approach (Reardon et al 2016, Wickersham et al

88   2007) to generate a presynaptic input map of V2M ttL5 neurons. Briefly, a mix of adeno-associated

89   viruses carrying floxed N2c G-protein, or TVA-receptor and EGFP genes were injected into V2M of

90   Colgalt2-Cre mice under stereotaxic guidance. Five to seven days later, mCherry expressing EnvA-CVS-

91   N2c-ΔG rabies virus was injected at the same location. After a further 10-12 days, brains were fixed and

92   imaged using serial section 2-photon tomography (Figure S2A). The resultant datasets were registered to

93   the Allen CCFv3 atlas and presynaptic cell bodies were detected and counted using an automated

94   pipeline (see Methods for details).
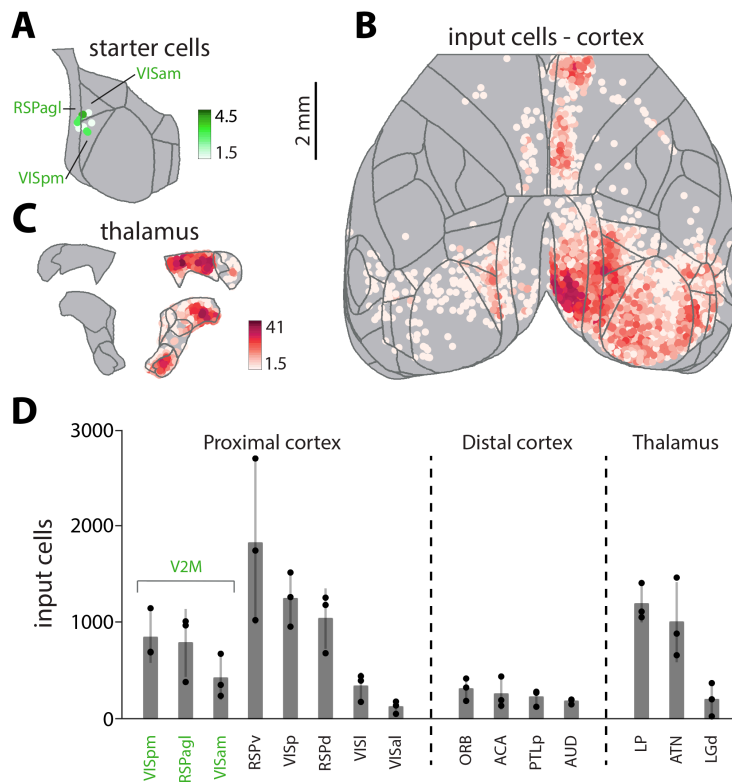
96   **Figure 1. Whole-brain input map to V2M ttL5 neurons. A.** Starter cell density map from an example experiment. **B.**

97   Cortical input cell density map projected onto the horizontal plane, same experiment as in A. **C.** Thalamic input cell

98   density map projected onto two coronal planes, same experiment as in A. Area names can be found in Figure S3;

99   density scales are in cells / 0.01 mm^2. **D.** Input cell numbers for the most prominent input areas. Averages, standard

100   deviation, and individual experiments are show.

101   Cell density maps for an example experiment are shown in Figure 1. Starter cells were scattered across

102   V2M (Figure 1A) while presynaptic input neurons were detected in a broad range of cortical and

103   subcortical areas (Figure 1B,C). We have grouped the most prominent input areas into proximal cortex,

104   distal cortex, and thalamus (Figure 1D). The majority of input cells were found locally in V2M and in the

105   proximal cortical areas VISp and the granular retrosplenial cortex (RSPg, consisting of RSPd and RSPv).

106   Orbitofrontal cortex (ORB) and the anterior cingulate area (ACA) provided the most numerous distal

107   cortical inputs. Interestingly, while most cortical input cells were detected in the granular and infragranular

108   layers, especially layer 5, input from ORB was almost exclusively from layer 2/3 (Figure S2BC).

109   Prominent thalamic inputs were also observed, originating mainly in the lateral posterior nucleus (LP) and

110   anterior thalamic nuclei (ATN). Comprehensive cell counts for individual experiments can be found in

111   Supplementary table 1.

112   To understand the organization of inputs onto ttL5 neurons in V2M, we chose to further examine 7

113   prominent input areas. VISp and V2M for FF input; RSPg, ACA and ORB for cortical FB input; and LP

114   and ATN for thalamic FB connections. We designate local (V2M) input as FF, as ttL5 neurons are

115   considered the outputs of the cortical column, and have very limited local projections.

Subcellular optogenetic input mapping reveals diverse targeting of dendritic domains by input areas

118   To determine the spatial distribution of synaptic inputs to ttL5 neurons in V2M, we performed sCRACM

119   experiments from selected input areas identified by the rabies tracing. Following expression of the

120   optogenetic activator Chronos in different input areas (see methods for injection details), we made

121   voltage-clamp recordings (at -70 mV) from tdTomato labelled (Colgalt2-Cre) ttL5 neurons in V2M using

122   acute brain slices. Optical stimulation with a 463 nm laser was spatially targeted using a digital

123   micromirror device (Figure 2A). Sodium and potassium channels were blocked using TTX (1μm) and 4-

124   AP (100 μm) to ensure that evoked currents were restricted to directly stimulated nerve terminals and to

125   enhance presynaptic release, respectively. The stimulus consisted of 24 x 12 spots of light in a 1000 x

126   500 μm grid aligned to the axis of the apical dendrite of the recorded neuron and covering the whole

127   depth of cortex. We also quantified the total input from a given connection by recording synaptic currents

128   evoked by full-field stimulation. To facilitate comparison between projections, we used the same laser

129   intensity across all experiments.

130   Synaptic strength at each location was estimated by measuring the area of evoked synaptic currents

131   (corresponding to charge; Figure 2B) and creating normalized 2D maps of the spatial distribution of inputs

132   (Figure 2C). Individual maps were then aligned (either to the pia or soma) and averaged. To quantify the

133   spatial location of inputs, we projected the average 2D maps in directions parallel (Figure 2C) or

134   perpendicular to the apical dendrite (Figure 2D). Furthermore, we defined the spatial distribution of the

135   three main dendritic compartments based on 11 morphologically reconstructed Colgalt2-Cre neurons

136   (Figure S4). Basal dendrites were defined as those originating at the soma, oblique dendrites as those

137   originating from the apical trunk before the main bifurcation (including the apical trunk itself), and apical

138   tuft dendrites as those originating after the bifurcation. As all three dendritic compartments have similar

139   spine densities (Romand et al 2011), the horizontal projection of the average morphology was used to

140   separate the contribution of each dendritic domain to the total synaptic input (Figure 2D).

141   One potential concern when recording distal synaptic currents from a somatic electrode is the effect of

142   attenuation on detectability of currents. In neurons with weaker overall input, this might result in distal

143   currents becoming too small to detect, thus biasing the input map towards the soma. We tested this by

144   examining the correlation between the location of synaptic input and the total synaptic charge evoked by

145 full-field stimulation (Figure S5). No correlation was found for any of the recorded areas, suggesting no

146 detection bias for distal inputs.
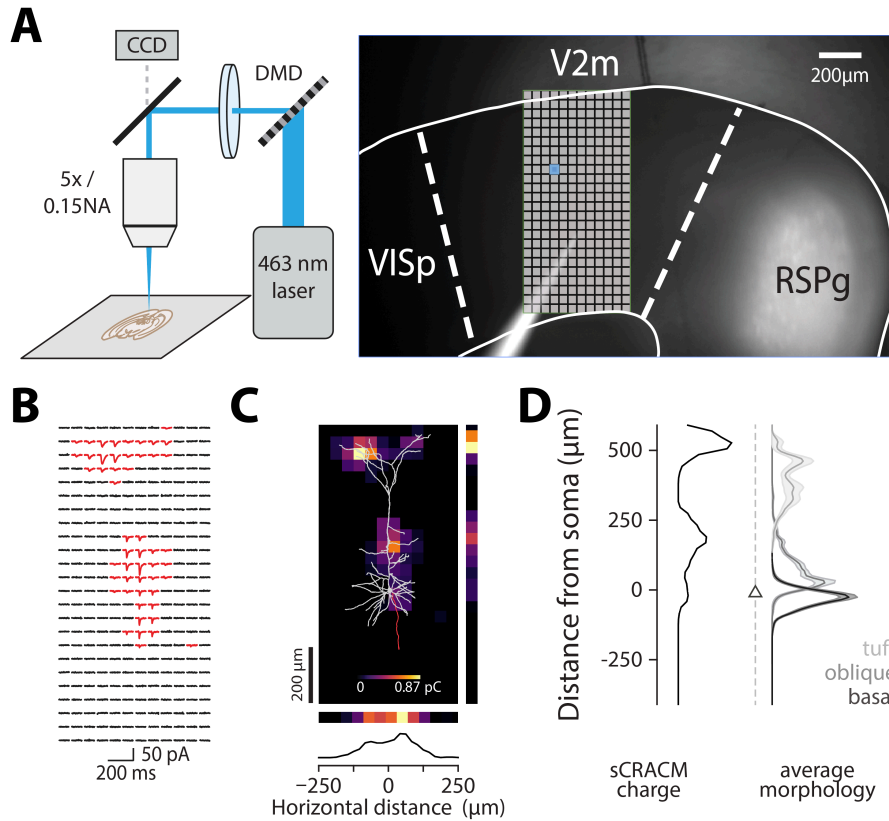
147

148 **Figure 2. Using sCRACM to map subcellular connectivity. A.** Experimental setup and micrograph showing a brain

149 slice with Chronos expression in RSPg and recording pipette in V2M. The stimulation grid is overlaid, and an example

150 spot is highlighted in blue. **B**. sCRACM recording of excitatory synaptic currents (red > 7 x baseline S.D.) from an

151 example neuron. **C.** Charge heatmap corresponding to recording in B with the morphology of the recorded neuron

152 overlaid. **D.** Normalized vertical profile of the input map in C. Right: average morphology profile used for dendritic

153 domain deconvolution.

Primary visual cortex

155 We first recorded optically evoked synaptic responses arising from VISp axons (n = 9 cells from 6

156 animals, average soma depth 507 ± 22 µm; Figure 3A). The apical tuft received 42% of the input, with a

157 peak input located 188 µm from the pia (Supplementary table 2). The remaining input was spread

158 between the oblique compartment, receiving 33%, and basal dendrites, receiving 26% of the total input.

159 More of the recorded neurons had the peak input in the apical compartment (n = 5 / 9) while 4 cells

160 lacked apical input (Figure S6). The horizontal input distribution showed a slight medial skew (towards

161 RSPg), most prominent in the oblique (63 µm) and basal compartments (42 µm; Figure S6B). The total

162 synaptic charge measured via the somatic recording following full-field stimulation was 0.93 ± 0.11 pC

163 (Figure 3A). VISp thus provides moderate direct input to ttL5 neurons in V2M, primarily targeting the

164 proximal part of the apical tuft (0.39 pC) with smaller input arriving to the oblique (0.30 pC) and basal

165 (0.24 pC) compartments.
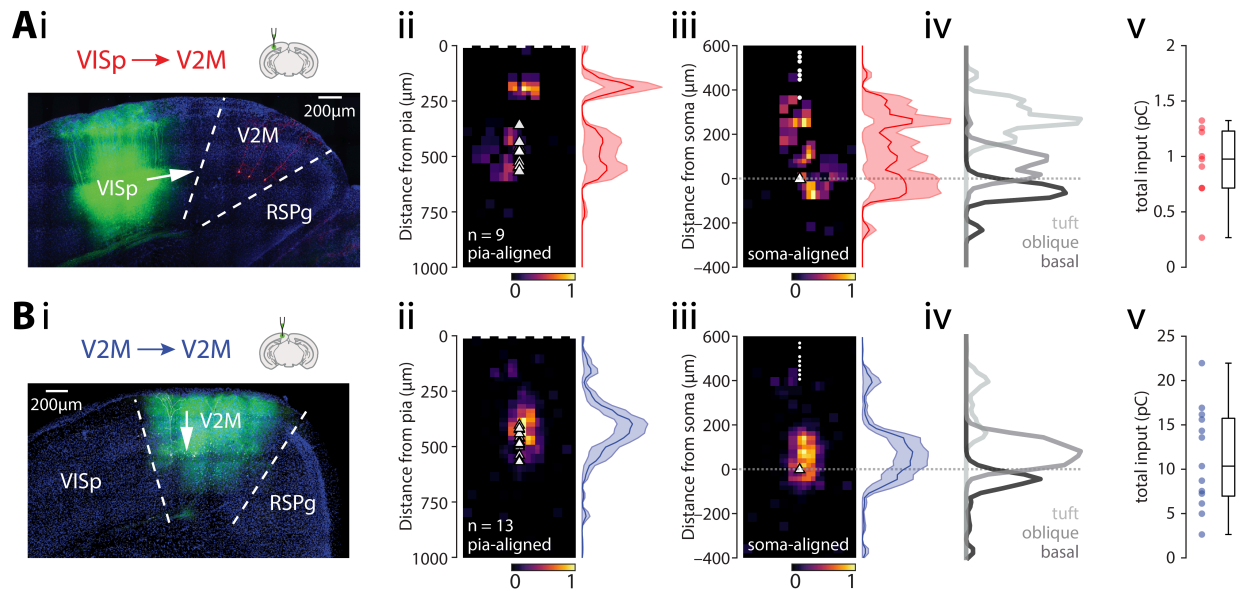
167 **Figure 3. Subcellular connectivity maps of FF input areas. A.** *i*: confocal image of a representative brain slice

168 (blue = DAPI) showing the injection site in VISp (green) and recorded neurons in V2M (red). *ii*: pia-aligned average

169 sCRACM heatmap for VISp inputs. Triangles represent soma locations. The vertical profile indicates the normalized

170 average and SEM of the input distributions across all recorded neurons. *iii*: Same as in ii but aligned on the soma

171 location. Dots indicate pia locations. *iv*: Normalized input magnitude deconvolved with the average morphology.

172 Dotted line indicates soma location. *v*: Box plot showing total input charge recorded during full-field stimulation. **B.**

173 Same as in A but for Cre-off Chronos injections into V2M.

Local input from V2M

175 To estimate the distribution of local input we used a Cre-off viral strategy, limiting Chronos expression to

176 non-Colgalt2-Cre neurons (n = 13 cells from 4 animals, average soma depth 498 ± 15 µm; Figure 3B).

177 When testing this strategy using the much denser Rbp4-Cre line, we found that only a very small

178 proportion of Cre-positive cells expressed Chronos (3%, Figure S7). The peak input was located close to

179 the soma, at 396 µm from the pia. The oblique compartment received the majority (62%) of this input, with

180 the basal dendrites and apical tuft receiving 24% and 14%, respectively, of the total input (Supplementary

181 table 2). For the majority of recorded neurons, the peak input occurred perisomatically (n = 12 / 13; Figure

182 S6C). The horizontal input distribution showed slight medial bias (-21 µm for all peaks; Figure S6D). The

183 total synaptic charge triggered by full-field stimulation was 11.24 ± 1.56 pC (Figure 3B). Local neurons

184 thus provide large direct input to ttL5 neurons in V2M, primarily targeting the oblique (6.96 pC)

185 compartment, with smaller input arriving to the basal (2.68 pC) and tuft (1.6 pC) compartments.

Granular retrosplenial area

Next, we recorded optically evoked synaptic responses arising from RSPg axons (n = 20 cells from 9 animals, average soma depth 503 ± 15 µm; Figure 4A). The overall input displayed a bimodal distribution peaking at 125 and 500 µm from the pia. The apical tuft received 30% of the input, with the oblique compartment receiving 40% and basal dendrites 30% of the total input (Supplementary table 2). For the majority of recorded neurons, the peak input targeted the perisomatic dendrites (n = 18 / 20; Figure S8A). The horizontal input distribution showed slight medial bias (Figure S8B). Total synaptic charge triggered by full-field stimulation was 3.40 ± 0.51 pC (Figure 4A). RSPg thus provides a relatively moderate direct input to ttL5 neurons in V2M, targeting the oblique (1.36 pC), basal (1.04 pC) and apical tuft (1.01 pC) compartments to similar extent.

Anterior cingulate area

Next, we recorded optically evoked synaptic responses arising from ACA axons (n = 23 cells from 5 animals, average soma depth 464 ± 9 µm; Figure 4B). The overall input was bimodal, peaking at 83 µm and 438 µm from the pia. The apical tuft received 25% of the input, with the oblique compartment receiving 45% and basal dendrites 30% of the total input (Supplementary table 2). The majority of recorded neurons had the peak input located perisomatically (n = 22 / 23; Figure S8C). The horizontal input distribution showed no medio-lateral bias (Figure S8D). The total synaptic charge triggered by full-field stimulation was 9.46 ± 1.32 pC (Figure 4B). ACA thus provides a large direct input to ttL5 neurons in V2M, primarily targeting the oblique (4.22 pC) compartment with smaller input arriving to the basal (2.83 pC) and most distal part of the apical tuft (2.41 pC).

Orbitofrontal cortex

Optically evoked synaptic responses arising from ORB axons (n = 11 cells from 3 animals, average soma depth 521 ± 19 µm; Figure 4C) showed a strong perisomatic bias, with a peak at 417 µm from the pia. The apical tuft received only 9% of all input, with the oblique compartment receiving 57% and basal dendrites 35% of the total input (Supplementary table 2). This distribution was also highly homogeneous across neurons, with almost all recorded neurons having their peak input in the perisomatic region (n = 11/11; Figure S8E). The horizontal input distribution showed no lateral bias (Figure S8F). The total synaptic charge triggered by full-field stimulation was 7.16 ± 1.43 pC (Figure 4C). ORB thus provides a large direct input to ttL5 neurons in V2M, primarily targeting the oblique (4.05 pC) and basal (2.47 pC) compartments, with slight input arriving to the proximal part of the apical tuft (0.63 pC).
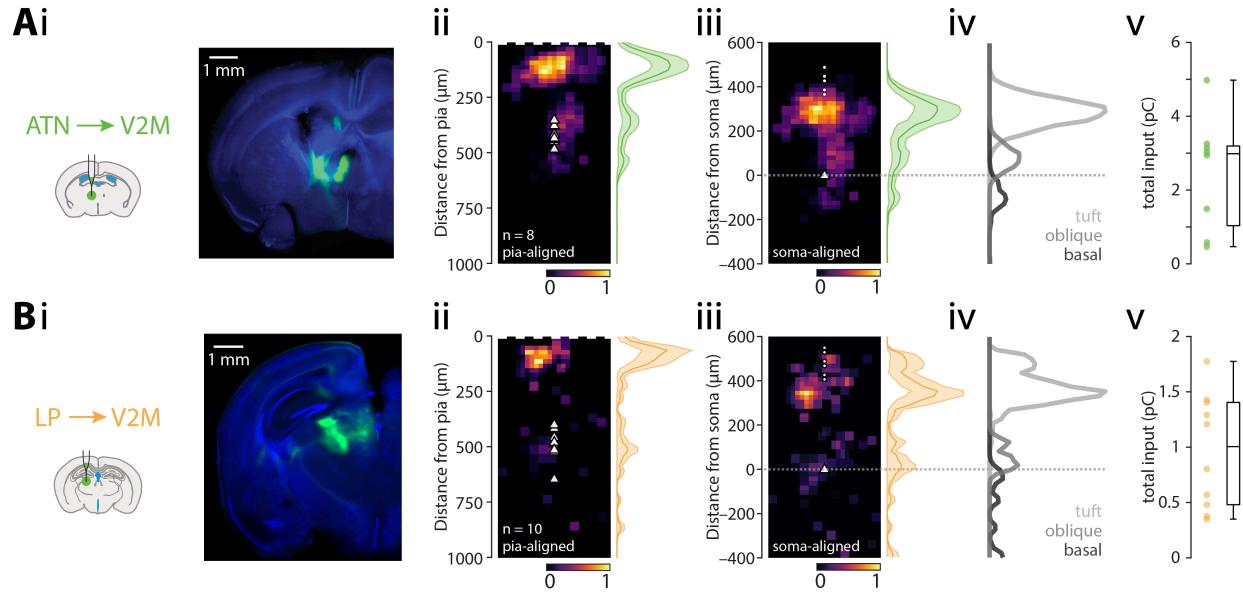
216
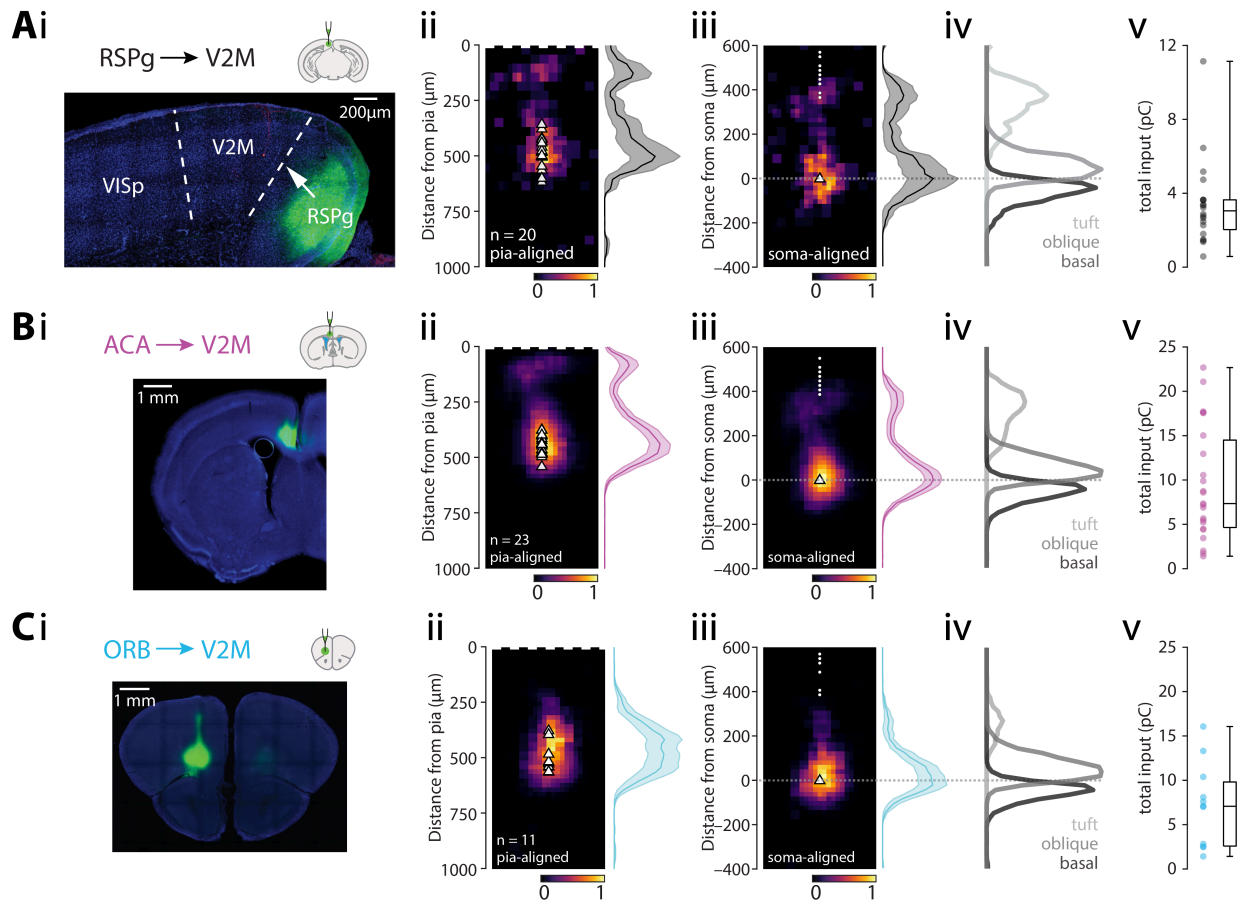
217

218 **Figure 4. Subcellular connectivity maps of cortical FB areas. A.** *i:* confocal image of a representative brain slice

219 (blue = DAPI) showing the injection site in RSPg (green). *ii:* pia-aligned average sCRACM heatmap for RSPg inputs.

220 Triangles represent soma locations. The vertical profile indicates the normalized average and SEM of the input

221 distributions across all recorded neurons. *iii:* Same as in *ii* but aligned on the soma location. Dots indicate pia

222 locations. *iv:* Normalized input magnitude deconvolved with the average morphology. Dotted line indicates soma

223 location. *v:* Box plot showing total input charge recorded during full-field stimulation. **B.** Same as in A but for Chronos

224 injections into ACA. **C.** Same as in A but for Chronos injections into ORB.

Anterior thalamic nuclei

226 Next, we recorded optically evoked synaptic responses from thalamic axons, starting with the ATN (n = 8

227 cells from 3 animals, average soma depth 435 ± 15 µm; Figure 5A). This input had peaks at both 104 µm

228 and 333 µm from the pia, with the apical tuft receiving the majority (75%) of the input, while the oblique

229 compartment received 17% and basal dendrites a mere 8% of the total input (Supplementary table 2).

230 The majority of recorded neurons had the peak input in the tuft compartment (n = 6 / 8) and while all cells

231 had some tuft input, in 2/8 cells the input peak was located perisomatically (Figure S9A). The horizontal

232 input distribution showed a medial bias (Figure S9B). The total synaptic charge triggered by full-field

233 stimulation was 2.48 ± 0.54 pC (Figure 5A). ATN thus provides a moderate direct input to ttL5 neurons in

234 V2M, primarily targeting the more distal part of the apical tuft (1.86 pC) while the oblique (0.42 pC) and

235 the basal (0.21 pC) compartment received less input.

236

237

238 **Figure 5. Subcellular connectivity maps of thalamic input areas. A.** *i:* confocal image of a representative brain

239 slice (blue = DAPI) showing the injection site in ATN (green). *ii:* pia-aligned average sCRACM heatmap for ATN

240 inputs. Triangles represent soma locations. The vertical profile indicates the normalized average and SEM of the

241 input distributions across all recorded neurons. *iii:* Same as in *ii* but aligned on the soma location. Dots indicate pia

242 locations. *iv:* Normalized input magnitude deconvolved with the average morphology. Dotted line indicates soma

243 location. *v:* Box plot showing total input charge recorded during full-field stimulation. **B.** Same as in A but for Chronos

244 injections in LP.


245 *Lateral posterior nucleus of the thalamus*

246 Lastly, we recorded optically evoked synaptic responses arising from LP axons (n = 10 cells from 4

247 animals, average soma depth 500 ± 23 µm; Figure 5B). Due to excessive retrograde labelling resulting in

248 direct photocurrent in the recorded V2M cells, a 1:10 dilution of virus was used for these injections and

249 the absolute value of the evoked input is thus likely an underestimate. As with ATN axons, the LP input

250 was strongly biased towards the most superficial part of the cortex and peaked at 63 µm from the pia. The

251 apical tuft received the vast majority (75%) of the input, with the oblique compartment receiving 15% and

252 basal dendrites 10 % of the total input (Supplementary table 2). Most recorded neurons had the peak

253 input in the tuft compartment (n = 9/10; Figure S9C). The horizontal input distribution showed lateral bias

254 (Figure S9D). The total synaptic charge triggered by full-field stimulation was 0.97 ± 0.16 pC (Figure 5B).

255 LP thus provides modest direct input to ttL5 neurons in V2M, primarily targeting the most distal part of the

256 apical tuft (0.72 pC) compartment with smaller input arriving to the oblique (0.14 pC) and the basal (0.10

257 pC) compartments.

Comparison of anatomical and functional connectivity maps

259 Having determined the spatial distribution of synapses for the main input areas, we next sought to directly

260 compare this to what would be predicted from axo-dendritic overlap (i.e. from Peters' rule). To determine

261 axonal projection patterns from input areas to V2M, we have imaged the Chronos-eGFP labelled axons in

262 a subset of the brain slices used for the sCRACM experiments using confocal microscopy.

263

264
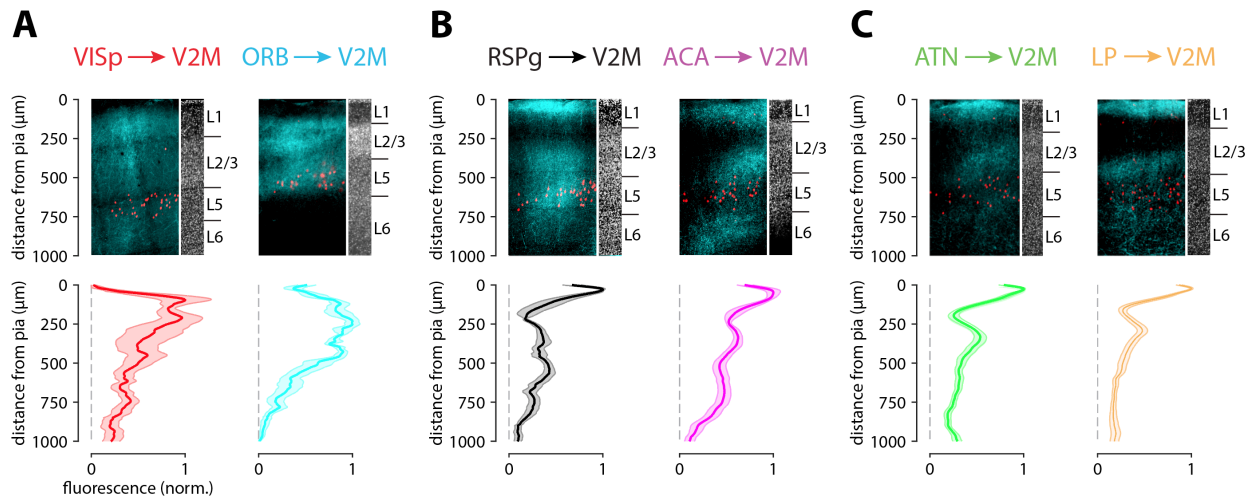
Figure 6. Axonal projection densities from different input areas. A-C. Top: example confocal images from V2M

showing axonal projections from six input areas (cyan) and Colgalt2-Cre cell bodies (red). The corresponding DAPI

staining shows variation in laminar depth. Bottom: average projection density profiles across the cortical depth

averaged across 3-5 injections.

269 The spatial distribution of axons followed three basic patterns. Axons from VISp and ORB were densest

270 in layer (L) 2/3 and L5 while little projection was apparent in L1, reminiscent of the classical FF projection

271 pattern (Figure 6A). In contrast, axons from RSPg and ACA showed an FB-like pattern with dense

272 labelling in the middle part of L1 followed by sparse labelling in L2 and diffuse axons in layers 3, 5 and 6

273 (Figure 6B). The final group, which consists of the thalamic projections from LP and ATN, showed the

274 classical FB pattern strongly innervating the external part of L1, with a secondary peak in L3, but little or

275 no projections in layers 2, 5 and 6 (Figure 6C).

276 To accurately estimate morphological overlap between axons and dendrites, we multiplied the axonal

277 projection maps with the average dendritic morphology, resulting in the predicted input distribution one

278 would expect to see based on Peters' rule. When overlaying this with the pia-aligned vertical sCRACM

279 maps, the alignments between functional synapses and the axo-dendritic maps were diverse (Figure 7A).

280   For some regions, like ORB perisomatic and LP tuft inputs, a clear correspondence could be seen

281   between predicted and measured input distributions. A lesser degree of overlap can be seen in the VISp

282   perisomatic or ACA tuft inputs. For other inputs, however, strong functional input could be detected where

283   there is little overlap between dendrites and axons, such as at VISp tuft inputs. This stood in stark

284   contrast to the ORB projection, for which the opposite was true, and apical regions of dense

285   morphological overlap of axons and dendrites resulted in no functional input.

286   Next we examined the correspondence between the anatomical input connectivity obtained from rabies

287   tracing and the functional connectivity measured by total synaptic input. The number of rabies-labelled

288   input neurons showed a strong contribution from RSPg and V2M, and modest input cell numbers for the

289   more distal cortical regions (e.g. ACA, ORB). The total synaptic input, however, shows no correlation with

290   these numbers (p = 0.8, r = -0.14, Spearman correlation, Figure 7B), with modest synaptic input from

291   RSPg and most input arriving from V2M, ACA and ORB. Taken together, these results show clear

292   specificity of dendritic targeting by brain-wide connections, with only a loose adherence to Peters' rule for

293   most inputs as well as large differences between anatomical and functional connectivity measured by

294   rabies tracing and optogenetic stimulation, respectively.

295

296
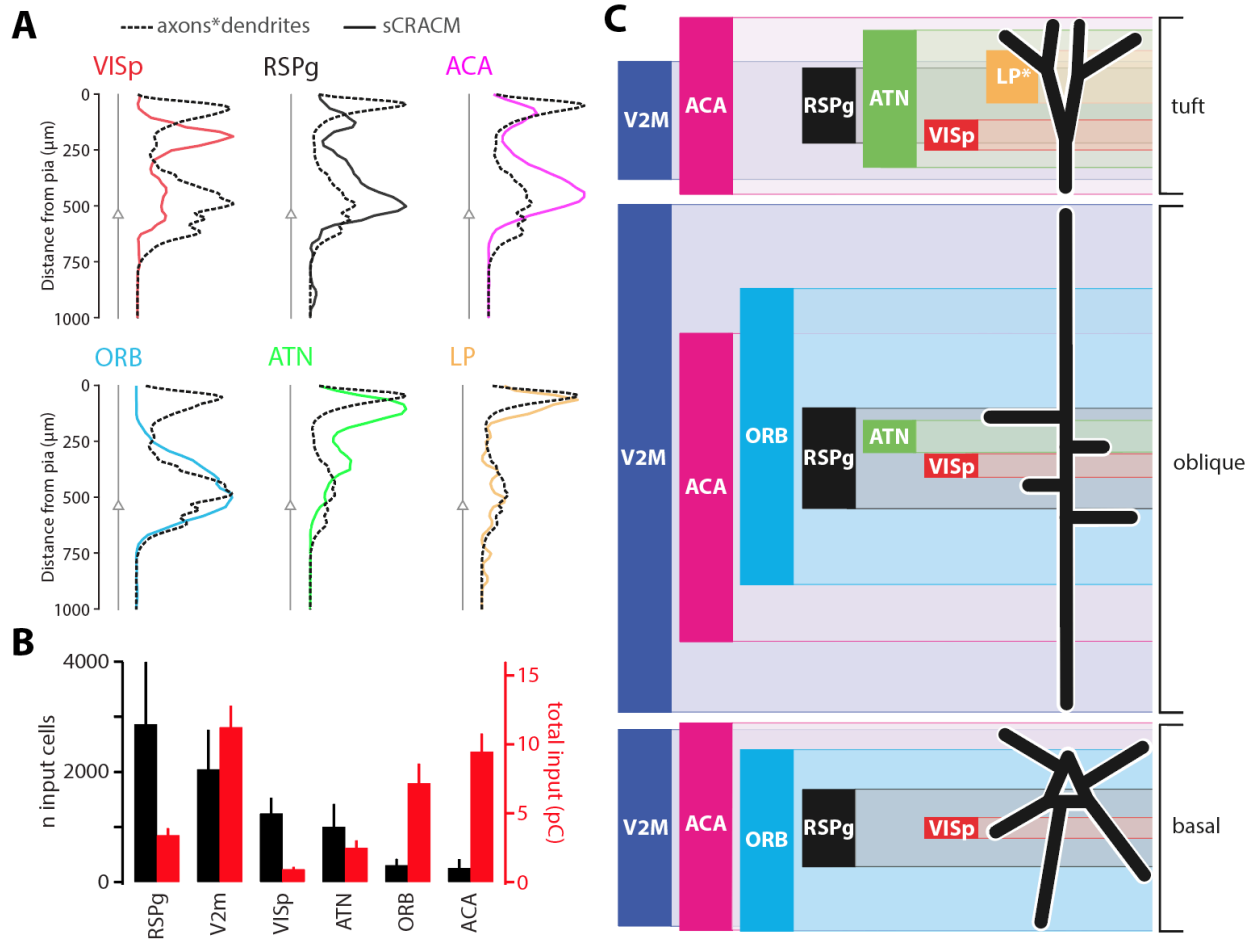
Figure 7. Comparison of different input maps. A. Axonal density distributions multiplied with dendritic morphology (dotted black lines) overlaid with pia-aligned synaptic input distributions (coloured lines). Six input areas are shown. Triangles represent soma location in average morphology. **B.** Number of input cells across 6 areas established by rabies tracing (black) and total input charge recorded during full-field optogenetic stimulation (red). **C.** Schematic of excitatory synaptic input map to ttL5 pyramidal neurons. The height of bars represents input strength, while the centre of each bar is aligned to the peak of the sCRACM map. The tuft input map was generated from pia aligned maps while oblique and basal maps from soma aligned maps. NB: LP input magnitude (*) is likely underestimated due to the lower virus titer used.

305

Discussion

306

307 Using an array of techniques for long-range circuit dissection, we have comprehensively mapped the

308 location and dendritic targets of inputs to ttL5 neurons in the medial secondary visual cortex in mice. This

309 allowed us to determine the dendritic targets of FF and FB connections and to make a direct assessment

310 of Peters' rule for brain-wide connections.

311 The whole-brain input map generated via rabies tracing was qualitatively similar to previous results from

312 the primary visual cortex (Kim et al 2015). Axonal projections from the rabies-identified input regions

313 broadly followed the expected pattern, with FB projections being biased toward L1 and FF areas toward

314 the deeper layers (D'Souza et al 2020, Harris et al 2019, Rockland & Pandya 1979). Accordingly, L1 was

315 densely innervated by higher-order cortical areas like RSPg and ACA as well as the secondary thalamic

316 nuclei (LP, ATN). Interestingly, ORB, a higher-order cortical region, displayed a projection pattern

317 associated with FF areas. Additionally, the majority of ORB projection neurons were found in L2/3,

318 another feature of FF connectivity. ORB thus seems to be an exception in terms of FB axonal projections.

319 Compared to the axonal projection patterns, synaptic input maps showed a remarkable degree of

320 heterogeneity. Morphological averaging was necessary as the sCRACM recordings in our dataset did not

321 have paired reconstructions for every cell. While it is possible that comparing the individual axon,

322 dendrite, and synaptic profiles on a single-cell basis would have given slightly more accurate results, the

323 overall pattern of functional input from each input region was mostly consistent across cells. Morphologies

324 of ttL5 neurons are likewise highly stereotypical. Furthermore, the axon projection patterns used for

325 evaluating Peters' rule were measured from a subset of the same slices used for the sCRACM

326 recordings, further supporting the direct comparison of the predicted input maps with those recorded

327 functionally. The discrepancy resulting from averaging is thus likely to be low. Indeed, any smoothing

328 resulting from averaging of morphologies, axonal projections or sCRACM maps would only increase

329 overlap, and thus bias the results in favor of adhering to Peters' rule. In contrast to this, several

330 connections showed only weak correspondence between predicted and observed input maps. The

331 connection from VISp, which is FF by definition and as such is assumed to primarily target perisomatic

332 dendrites (Larkum 2013), was instead biased towards the apical tuft. Conversely, while the axons from

333 ORB had a FF-like projection pattern, they synapsed almost exclusively with basal and oblique dendrites.

334 Other recorded areas (e.g., RSPg, ACA, ATN) showed some degree of conformity to Peters' rule, yet still

335 with significant differences in the proportion of synapses generated in the different regions of high axonal

336 projections. The only area where the correspondence was remarkable and Peter's rule held fully was LP.

337 Comparing anatomical connectivity obtained by rabies tracing to functional connectivity obtained by full-

338 field optogenetic stimulation of axons revealed large and unexpected differences. When evaluating this

339 finding, it is important to consider a few technical caveats which might bias this comparison. First, while

340 we have not found false-positive areas (i.e., every area revealed by rabies tracing and tested by sCRACM

Dendritic distribution of synaptic inputs to layer 5 pyramidal neurons

341   provided input), there is considerable debate regarding the quantitative accuracy of rabies tracing

342   (Rogers & Beier 2021). Second, the magnitude of optogenetically evoked input depends on the number of

343   presynaptic cells covered by viral injection. To facilitate comparison with the rabies labelling, we aimed to

344   maximise coverage of each area by making several injections targeted to the locations with the highest

345   density in the rabies data. It is unlikely that these technical caveats could alone account for the

346   remarkable discrepancy between anatomical and functional input magnitudes. There are several other

347   possible explanations for this difference. First, there may be differing convergence of connectivity

348   between input areas. For example, low convergence in inputs with strong rabies labelling, with a unique

349   mapping of selected pre- and postsynaptic cells, could result in relatively weaker sCRACM input (like

350   VISp and RSPg). Meanwhile, strong synaptic currents relative to small rabies-labelled populations (like

351   ORB and ACA) may be explained by higher convergence. Such connections might be less discerning of

352   their targets in order to convey more general contextual or state-specific information. Second, there may

353   be a difference in the strength of individual synapses not reflected in rabies efficiency, with sparsely

354   labelled input areas like ORB having relatively strong synapses, while rabies-dense areas like RSPg may

355   send a large number of weaker synapses. A third contributing factor could be the recently reported

356   activity-dependence of rabies transmission (Beier et al 2017). The apparent sparsity of some input areas

357   (like ORB and ACA) could thus arise from having very low activity. Conversely, to result in extensive

358   rabies labelling, VISp and RSPg should provide high activity input.

359   We used a novel approach to allocate sCRACM input to specific dendritic compartments by deconvolving

360   the synaptic input maps using morphological ttL5 reconstructions in which we manually labelled tuft,

361   oblique, and basal compartments. Our results provide a complex picture regarding the possible

362   interaction of FF and FB inputs (Figure 7C). Functionally, V2M has been linked to visual motion

363   processing (Sun et al 2009) and is thought to take part in navigation and spatial processing as part of the

364   dorsal stream (Glickfeld & Olsen 2017). Thalamic FB input, which targets almost exclusively the apical

365   tuft, arrives from multiple higher-order nuclei. Parts of ATN receive strong vestibular input (Rancz et al

366   2015) and, together with RSP form a central part of the head-direction system (Taube 2007, Velez-Fort et

367   al 2018). It is thus likely that spatial and multisensory contextual information carried by LP inputs (Roth et

368   al 2016) interacts with FF visual input in the tuft compartment. However, the role of tuft integration is likely

369   to differ from primary sensory cortices, considering that ttL5 neurons in the secondary visual cortex have

370   substantially different integrative properties (Galloni et al 2020). Contrary to thalamic input, cortical FB

371   inputs target all three dendritic domains. Perhaps surprisingly, the strongest of these are ORB and ACA,

372   which can interact with the local FF input at the level of oblique and basal dendrites. Frontal cortices in

373   general are involved in decision making and executive control of behavior (Hamilton & Brigman 2015),

374   and ORB in particular has been shown to encode spatial goals (Feierstein et al 2006). ACA, meanwhile,

375   can directly regulate visually evoked responses and sensory discrimination in the primary visual cortex

376   (Zhang et al 2014), and contributes to learning to predict sensory input to primary visual cortex (Fiser et al

377   2016). Their precise roles in the functioning of V2M, however, remains unknown. The strong input

378   received by oblique dendrites is particularly important, as this compartment was shown to strongly affect

379   L5 excitability (Schaefer et al 2003) and can gate information flow from the apical dendrites (Jarsky et al

380   2005). While FB inputs targeting the apical tuft have been suggested to act as a general gain control for

381   ttL5 neurons, it is thus possible that ORB and ACA perform a similar gating function, but perhaps with

382   more specificity regarding input identity or dendritic branches. Indeed, their particularly strong targeting of

383   oblique dendrites might allow both fine-level control of plasticity for FF synapses at these dendrites, while

384   simultaneously allowing them to exert gating control over input from both the thalamic nuclei and VISp,

385   which strongly project to the tuft.

386   In general, our results show that while the classification of areas as FF or FB can be based on axonal

387   projections (albeit with exceptions, such as ORB), macroscopic projectomes do not predict cell-type level

388   input location, and individual connections do not follow clear rules associated with their position above or

389   below the target area in a cortical hierarchy. Similarly, while rabies tracing from a population of starter

390   cells is an effective tool to study the general wiring diagram, the proportion of input neurons thus

391   estimated is likely to give a poor estimation of functional input strength. Finally, the location and possible

392   interactions between FF and the broad range of FB inputs as well as their specific information content

393   suggests that ttL5 neurons may be adopting a multitude of integrative strategies that are more complex

394   than those previously suggested.

Materials and Methods

Animals

All animal experiments were prospectively approved by the local ethics panel of the Francis Crick Institute (previously National Institute for Medical Research) and the UK Home Office under the Animals (Scientific Procedures) Act 1986 (PPL: 70/8935). All surgery was performed under isoflurane anesthesia, and every effort was made to minimize suffering. Transgenic mice were used: Tg(Colgalt2-Cre)NF107Gsat (RRID:MMRRC_036504-UCD, also known as Glt25d2-Cre) were crossed with the Ai14 reported line expressing tdTomato (RRID:IMSR_JAX:007908). Additionally, Tg(Rbp4-Cre)KL100Gsat/Mmucd (RRID:MMRRC_031125-UCD) mice were used to establish the efficacy of the cre-off approach. As only male mice are transgenic in the Colgalt2-Cre line, all experiments were done on male animals. Animals were housed in individually ventilated cages under a 12 hr light/dark cycle.

Viruses

EnvA-CVS-N2c$^{\Delta G}$-mCherry rabies virus, and adeno associated viruses expressing TVA and EGFP (AAV8-EF1a-flex-GT), N2c glycoprotein (AAV1-Syn-flex-H2B-N2CG), or Cre-OFF Chronos-GFP (AAV1-EF1-CreOff-Chronos-GFP) were a generous gift of Molly Strom and Troy Margrie. Chronos-GFP (also called ShChR) expressing adeno associated virus (rAAV1-Syn-Chronos-GFP) was obtained from UNC Vector Core.

Surgical procedures

Surgeries were performed on mice aged 3–8 weeks using aseptic technique under isoflurane (2–4%) anesthesia and analgesia (meloxicam 2 mg/kg and buprenorphine 0.1 mg/kg). The animals were head-fixed in a stereotaxic frame and a small hole (0.5–0.7 mm) was drilled in the skull above the injection site. Virus was loaded into a glass microinjection pipette (pulled to a tip diameter of around 20 μm) and pressure injected into the target region at a rate of 0.4 nl/s using a Nanoject III delivery system (Drummond Scientific). To reduce backflow, the pipette was left in the brain for approximately 5 min after completion of each injection.

For rabies virus tracing experiments, a 1:2 mixture of TVA and N2c glycoprotein expressing cre-dependent AAVs (10-20 nL) was injected at stereotaxic brain coordinates (λ - 0.8 mm, ML 1.6 mm, DV 0.6 mm). Rabies virus (50-100 nL) was injected 5-7 days later at the same site. Ten to twelve days later, animals were transcardially perfused under terminal anesthesia with cold phosphate-buffer (PB, 0.1 M) followed by 4% paraformaldehyde (PFA) in PB (0.1 M).

For the sCRACM experiments, Chronos-GFP expressing AAV was injected into one of the identified presynaptic regions. The virus was allowed to express for at least 3 weeks before acute brain slice

427   preparation. The range of stereotaxic coordinates for each region are listed in Supplementary table 3. The

428   injected virus was Chronos-GFP for every region except V2M, where Cre-OFF Chronos-GFP was instead

429   used to avoid expression in the recorded Colgalt2-Cre neurons. For some of the injections in LP, the

430   Chronos-GFP virus was diluted by 10-fold in sterile cortex buffer before injection.

431   *Data acquisition and analysis for rabies tracing experiments*

432   Brain samples were embedded in 4-5% agarose (Sigma-Aldrich: 9012-36-6) in 0.1M PB and imaged

433   using serial two-photon tomography (Han et al 2018, Osten & Margrie 2013, Ragan et al 2012). Eight

434   optical sections were imaged every 5 μm with 1.2 μm x 1.2 μm lateral resolution, after which a 40μm

435   physical section was removed. Excitation was provided by a pulsed femto-second laser at 800 nm

436   wavelength (MaiTai eHP, Spectraphysics). Images were acquired through a 16X, 0.8 NA objective (Nikon

437   MRP07220) in three channels (green, red, blue) using photomultiplier tubes. Image tiles for each channel

438   and optical plane were stitched together with an open-source software written in MATLAB

439   (https://github.com/SainsburyWellcomeCentre/StitchIt). For cell detection, full resolution images were first

440   filtered with a Gaussian blur (sigma = 1) using Fiji (ImageJ 1.52e) to reduce imaging noise. The open-

441   source package "cellfinder" (Tyson et al 2020) was used for cell candidate detection then classification.

442   Automated mouse atlas propagation (Niedworok et al 2016) was used for registration and segmentation

443   on brain samples down-sampled to 10 μm voxels (to match the resolution of the Allen CCFv3; (Wang et al

444   2020a). Cell coordinates were similarly down-sampled to 10 μm and the number of cells was counted for

445   each segmented area. For cell density visualisation, cell coordinates were reverse-transformed onto the

446   Allen CCFv3 space using the open source registration tool, Elastix (Klein et al 2010) and were projected

447   onto a 2D matrix in 10 μm / pixel resolution.

448   *Acute slice preparation and electrophysiological recordings*

449   Adult mice were deeply anaesthetised with isoflurane and decapitated. The brain was rapidly removed

450   and placed in oxygenated ice-cold slicing solution containing (in mM): 125 sucrose, 62.5 NaCl, 2.5 KCl,

451   1.25 NaH_2PO_4, 26 $NaHCO_3$, 2 $MgCl_2$, 1 $CaCl_2$, 25 dextrose; osmolarity 340–350 mOsm. The cerebellum

452   and frontal cortex were removed manually with a coronal cut using a single-edged razor blade and the

453   rostral surface was affixed to a metal platform with cyanoacrylate glue. Coronal slices (300 μm thick)

454   between 2.6 and 3.5 mm posterior to bregma were prepared using a vibrating blade microtome (Leica

455   VT1200S). Slices were kept submerged in artificial cerebrospinal fluid (ACSF, containing in mM: 125

456   NaCl, 2.5 KCl, 1.25 NaH_2PO_4, 26 $NaHCO_3$, 1 $MgCl_2$, 2 $CaCl_2$, 25 dextrose; osmolarity 308–312 mOsm) at

457   35°C for the first 30–60 min after slicing, then at room temperature (22°C). All solutions and chambers

458   were continuously bubbled with carbogen (95% O2 / 5% CO2).

459   The topology of the cortical mantle in the region of V2m is curved and varies in thickness along the

460   antero-posterior axis. In most coronal sections, the apical dendrites of L5 neurons were thus at a slight

461   angle relative to the slicing surface. This angle was minimized by slicing the brain with a slight backward

462   angle relative to the coronal plane. Additionally, to avoid recording from neurons with cut apical dendrites,

463   slices were placed such that the apical dendrites could be seen to descend at a shallow angle into the

464   slice. Where possible, the fluorescently-labelled apical dendrites were also visually inspected along their

465   full path from soma to pia. Furthermore, many neurons were successfully filled with biocytin during

466   recording, making it possible to verify the integrity of the apical dendrite after the recordings. The

467   observed neurons were all found to have an intact apical trunk with tuft dendrites extending to the pia.

468   However, we can't exclude that a small fraction of finer dendrites (including both basal and apical tuft)

469   extending towards the slice surface may have been partially cut in the process.

470   For recordings, individual slices were perfused in the recording chamber at a rate of approximately 6

471   mL/min with ACSF at room temperature (22°C), continuously bubbled with carbogen. To prevent axonal

472   spike propagation and enhance responses to optical stimulation, 1 µM tetrodotoxin (TTX) and 100 µM 4-

473   aminopyridin (4-AP) were added to the recording ACSF. This ensured that any light-evoked responses

474   were direct monosynaptic responses resulting from stimulation of Chronos-expressing axon terminals,

475   rather than from passing axons terminating in unknown locations on the dendrites.

476   Filamented borosilicate thick-walled glass micropipettes were pulled and heat-polished using a two-stage

477   horizontal puller (Zeitz DMZ Universal Electrode Puller) to obtain an electrode resistance of 3–6 MΩ. The

478   glass electrodes were filled with internal solution optimized for voltage clamp recordings, containing (in

479   mM): 120 CsMeSO$_3$ (CH$_3$O$_3$SCs), 3 CsCl, 10 HEPES, 1 EGTA, 4 Na$_2$ATP, 0.3 NaGTP, 5 Na$_2$-

480   phosphoreatine (C$_4$H$_8$N$_3$O$_5$PNa$_2$), 3.5 QX-314 chloride, 0.5 % (w/v) biocytin hydrochloride, 50 µM Alexa

481   Fluor 488 hydrazide; osmolarity 290–295 mOsm; pH adjusted to 7.3 with CsOH.

482   Visually guided whole-cell patch-clamp recordings from tdTomato-labelled Colgalt2-Cre neurons in V2M

483   were performed using a Scientifica SliceScope Pro 3000 microscope equipped with a 40x/0.8 NA

484   objective and an infrared (IR) Dodt Gradient Contrast system. The epifluorescence system used to

485   visualize fluorescent neurons was a CoolLED pE-4000 illumination system with a 550 nm peak excitation

486   wavelength. To avoid stimulating Chronos-expressing axons, epifluorescent illumination was kept to a

487   minimum during selection of cells to record. Recordings were made with a Multiclamp 700B amplifier

488   (Molecular Devices) in voltage-clamp configuration with a holding potential of -70 mV. Filtered signals

489   (8kHz low-pass) were digitized at 20 kHz with a National Instruments DAQ board (PCIe-6323). Acquisition

490   and stimulus protocols were generated in Igor Pro (Wavemetrics) with the NeuroMatic software package

491   (Rothman & Silver 2018). Throughout each recording, series resistance compensation was applied and

492   set to the highest value possible without inducing oscillations in the cell (typically between 40 and 75%).

493   Recordings wtih series resistance larger than 40 MΩ were excluded.

494 *Patterned optogenetic stimulation*

495 Optical stimulation was implemented using a digital micromirror device (DMD) with a 463 nm laser (laser-
496 coupled Polygon 400, Mightex Systems). The stimulus consisted of a 1000 x 500 μm grid divided into 24
497 x 12 spots of light (41.7 μm x 41.7 μm square) delivered through a 5x/0.15 NA dry objective (Olympus
498 MPlanFL N). The grid was approximately centered on the soma being recorded from, aligned to the pia
499 orthogonal to the apical dendrite. For each individual spot, the laser power was measured at the
500 specimen plane using a PM100D (Thorlabs) optical power meter equipped with a S121C sensor
501 (Thorlabs). The laser output associated with each spot was adjusted to obtain a measured power of
502 approximately 300 μW (173 mW/mm2).

503 Optical stimuli were delivered for 1 ms at 0.1 Hz in a pseudo-random sequence designed to maximise the
504 distance between consecutive spots and the time between stimulation of neighbouring spots. Each
505 recording trial consisted of a single repetition of all 288 stimuli followed by a full-field stimulus, in which all
506 stimulation spots were illuminated simultaneously for 1 ms. For each cell, 5-20 trials were recorded, with
507 30s pauses between trials, making the interval between consecutive stimulation of the same spot
508 approximately 60s. Following each recording, an image was taken to record the location of the recorded
509 cell (filled with Alexa Fluor 488) relative to the stimulation grid. This was used during analysis to align the
510 recorded sCRACM heatmap with the location of the pia or soma.

511 *Immunohistochemistry & morphological reconstructions*

512 After recording, slices were fixed overnight at 4°C in a 4% paraformaldehyde solution and were
513 subsequently kept in PBS. Slices were stained with DAPI (5 μg/mL) for 10 min, mounted on glass slides
514 and images were acquired with either a confocal microscope for high-resolution images (Leica SP5;
515 objective: 20x/0.7NA or 10x/0.4NA; pinhole size: 1 airy unit) or a slide scanner for visualizing injection
516 sites (Olympus VS120, objective: 4x/0.16NA). Image processing was done with the FIJI software package
517 (Schindelin et al 2012). For the detailed morphological analysis, a subset of neurons, selected based on
518 the quality and completeness of staining, was reconstructed in full through the LMtrace service of
519 https://ariadne.ai/lmtrace.

520 *Comparison of axonal projection patterns to VISam, VISpm and RSPagl*

521 We have obtained layer-wise axonal projection data from the 6 input areas (ACA n=33, ATN n=11, LP
522 n=10, ORB n=11, RSPg n=17, VISp n=60) from the Allen Mouse Brain Connectivity database (© 2011
523 Allen Institute for Brain Science. Allen Mouse Brain Connectivity Atlas. Available from:
524 https://connectivity.brain-map.org/). Projection energy distributions were qualitatively similar across target
525 areas (Figure S1). Quantitatively, the data followed the same layer-wise pattern across the three target
526 areas (p > 0.05, 2-way ANOVA with Tukey's post hoc test) with the exception of ACA (RSPagl vs VISpm
527 p = 0.001; VISam vs VISpm p = 0.016). When only wild-type data was considered, no statistical

528   difference between target areas was detected (p > 0.05, 2-way ANOVA with Tukey's post hoc test; n =

529   ACA 5, ATN 4, LP 2, ORB 2, RSPg 2, VISp 21).

530   *Data analysis*

531   Analysis and data visualization were performed with custom macros and scripts written in Igor Pro and

532   MATLAB (Mathworks). Unless otherwise specified, all reported data values refer to the mean ± standard

533   error (SEM). Recordings were not corrected for liquid junction potential.

534   Recordings were baselined in a 40 ms window before each stimulus and averaged across trials, and the

535   peak and area of the evoked currents were measured in a 50 ms window after the stimulus. Stimulus

536   spots for which the peak current was lower than seven times the standard deviation of the baseline noise

537   were scored as zero.

538   For some of the injection sites, a degree of retrograde transport of the Chronos virus was noted in areas

539   outside of the primary injection site, including in V2M. A few recorded Colgalt2-Cre neurons in V2M were

540   thus found to be intrinsically expressing Chronos. This was easily detected in the recordings by an

541   instantaneous inward current at the onset of laser stimulation, in contrast to the 4-5 ms delay between

542   stimulus onset and sCRACM current observed normally. Any cells with no such delay were excluded from

543   the analysis.

544   Because peak response amplitudes varied between cells and preparations, to obtain average input

545   distributions from a presynaptic population, the heatmap for each cell was normalised to the peak EPSC

546   value for that cell. Heatmaps were then aligned horizontally by soma location and then vertically by either

547   soma or pia location before averaging each pixel across cells. For each cell, the soma could be localised

548   to within one quadrant of a given stimulation spot. When averaging across cells, the effective sampling

549   resolution (i.e. the pixel dimension) for the average sCRACM heatmaps and related horizontal and

550   vertical projections were thus approximately 20.8 µm (equal to half of the stimulus spot size, i.e. 1000/48

551   µm). All values reported for the locations of sCRACM inputs from different presynaptic regions are in

552   multiples of this number. Note, however, that the actual resolution with which synapses can be localised

553   in the heatmaps is likely to be lower than this, as it is limited by both light scattering in the tissue and by

554   the spread of voltage along stimulated axons, which is determined by the length constant of presynaptic

555   axons. Previous studies have indicated that these factors limit the actual sCRACM resolution to

556   approximately 60 µm (Petreanu et al 2009).

557   To estimate the proportion of sCRACM input targeting different dendritic domains, the recorded input map

558   for each cell was convolved with the average ttL5 morphology obtained from 11 reconstructed Colgalt2-

559   Cre neurons in V2M. This was done by manually separating the apical tuft, oblique (including the apical

560   trunk), and basal dendrites of the reconstructions in Neurolucida 360 and quantifying the total dendritic

561   length in 10 µm thick sections perpendicular to the main axis of the apical dendrite. The resulting dendrite

562   profiles were then aligned by the soma and averaged. Using this average morphology, at each distance

Dendritic distribution of synaptic inputs to layer 5 pyramidal neurons   21

563   from the soma the proportion of dendrites belonging to each domain was calculated relative to the total

564   dendritic length within that section. For each sCRACM recording, these proportions were calculated using

565   an average morphology that was scaled to the soma-pia distance of the recorded cell. Each pixel of the

566   heatmap for that cell was then multiplied by these dendritic proportions to obtain the proportion of evoked

567   current assigned to each dendritic domain. Averaging the morphological reconstructions was necessary

568   because only a small fraction of the recorded neurons was fully reconstructed, and we were thus unable

569   to allocate sCRACM measures to specific dendritic domains on a cell-by-cell basis. Notably, because of

570   variation in apical dendrite length between different ttL5 neurons, the choice of soma alignment before

571   averaging the morphologies resulted in the average morphology profile having a graded rather than sharp

572   cutoff at the pia. The peak dendrite density near the pia thus appears smaller than it would in a pia-

573   aligned average and is not related to any loss of dendrites in the reconstructed neurons. This choice was

574   made because the distribution of tuft dendrites had relatively little overlap with the other dendritic

575   domains, resulting in a more accurate assignment of sCRACM inputs to each domain. Had we aligned

576   the morphologies by the pia instead, the resulting distributions for basal and oblique dendrites would have

577   far greater overlap, resulting in lower accuracy in the dendritic domain classification.

578   The average morphology profile was also used to quantify the expected input profile on the basis of axon

579   and dendrite densities at each distance from the pia. In this case, however, the same reconstructed

580   morphologies were instead aligned by the apical tuft before averaging, in order to make the predicted

581   input more comparable to the pia-aligned sCRACM maps. As with the sCRACM input, pia-alignment

582   resulted in greater definition at the pia at the cost of reduced resolution near the average soma location.

583   Following alignment, both the axon and dendrite distributions were normalized to the peak of each curve

584   and multiplied, resulting in large values for expected input at locations containing both axons and

585   dendrites.

586

Acknowledgments

587

591   **Competing interests:** The authors declare that no competing interests exist.

592

References

Anastasiades PG, Collins DP, Carter AG. 2021. Mediodorsal and Ventromedial Thalamus Engage Distinct L1 Circuits in the Prefrontal Cortex. *Neuron* 109: 314-30 e4

Aru J, Suzuki M, Larkum ME. 2020. Cellular Mechanisms of Conscious Processing. *Trends Cogn Sci* 24: 814-25

Beier KT, Kim CK, Hoerbelt P, Hung LW, Heifets BD, et al. 2017. Rabies screen reveals GPe control of cocaine-triggered plasticity. *Nature* 549: 345-50

Briggman KL, Helmstaedter M, Denk W. 2011. Wiring specificity in the direction-selectivity circuit of the retina. *Nature* 471: 183-8

Collins DP, Anastasiades PG, Marlin JJ, Carter AG. 2018. Reciprocal Circuits Linking the Prefrontal Cortex with Dorsal and Ventral Thalamic Nuclei. *Neuron* 98: 366-79 e4

D'Souza RD, Meier AM, Bista P, Wang Q, Burkhalter A. 2016. Recruitment of inhibition and excitation across mouse visual cortex depends on the hierarchy of interconnecting areas. *Elife* 5

D'Souza RD, Wang Q, Ji W, Meier AM, Kennedy H, et al. 2020. Canonical and noncanonical features of the mouse visual cortical hierarchy. *biorxiv.org*

Feierstein CE, Quirk MC, Uchida N, Sosulski DL, Mainen ZF. 2006. Representation of spatial goals in rat orbitofrontal cortex. *Neuron* 51: 495-507

Felleman DJ, Van Essen DC. 1991. Distributed hierarchical processing in the primate cerebral cortex. *Cereb Cortex* 1: 1-47

Fino E, Yuste R. 2011. Dense inhibitory connectivity in neocortex. *Neuron* 69: 1188-203

Fiser A, Mahringer D, Oyibo HK, Petersen AV, Leinweber M, Keller GB. 2016. Experience-dependent spatial expectations in mouse visual cortex. *Nat Neurosci* 19: 1658-64

Franklin KBJ, Paxinos G. 2007. *Paxinos and Franklin's The mouse brain in stereotaxic coordinates*. Amsterdam: Academic Press, an imprint of Elsevier. 1 volume (unpaged) pp.

Galloni AR, Laffere A, Rancz E. 2020. Apical length governs computational diversity of layer 5 pyramidal neurons. *Elife* 9

Garrett ME, Nauhaus I, Marshel JH, Callaway EM. 2014. Topography and areal organization of mouse visual cortex. *J Neurosci* 34: 12587-600

Glickfeld LL, Olsen SR. 2017. Higher-Order Areas of the Mouse Visual Cortex. *Annu Rev Vis Sci* 3: 251-73

Groh A, Meyer HS, Schmidt EF, Heintz N, Sakmann B, Krieger P. 2010. Cell-type specific properties of pyramidal neurons in neocortex underlying a layout that is modifiable depending on the cortical area. *Cereb Cortex* 20: 826-36

Guerguiev J, Lillicrap TP, Richards BA. 2017. Towards deep learning with segregated dendrites. *Elife* 6

Hamilton DA, Brigman JL. 2015. Behavioral flexibility in rats and mice: contributions of distinct frontocortical regions. *Genes Brain Behav* 14: 4-21

Han Y, Kebschull JM, Campbell RAA, Cowan D, Imhof F, et al. 2018. The logic of single-cell projections from visual cortex. *Nature* 556: 51-56

Harris JA, Mihalas S, Hirokawa KE, Whitesell JD, Choi H, et al. 2019. Hierarchical organization of cortical and thalamic connectivity. *Nature* 575: 195-202

Helmstaedter M, Briggman KL, Turaga SC, Jain V, Seung HS, Denk W. 2013. Connectomic reconstruction of the inner plexiform layer in the mouse retina. *Nature* 500: 168-74

Hooks BM, Mao T, Gutnisky DA, Yamawaki N, Svoboda K, Shepherd GM. 2013. Organization of cortical and thalamic input to pyramidal neurons in mouse motor cortex. *J Neurosci* 33: 748-60

Hubel DH, Wiesel TN. 1962. Receptive fields, binocular interaction and functional architecture in the cat's visual cortex. *J Physiol* 160: 106-54

Jarsky T, Roxin A, Kath WL, Spruston N. 2005. Conditional dendritic spike propagation following distal synaptic activation of hippocampal CA1 pyramidal neurons. *Nat Neurosci* 8: 1667-76

Kasthuri N, Hayworth KJ, Berger DR, Schalek RL, Conchello JA, et al. 2015. Saturated Reconstruction of a Volume of Neocortex. *Cell* 162: 648-61

Kim EJ, Juavinett AL, Kyubwa EM, Jacobs MW, Callaway EM. 2015. Three Types of Cortical Layer 5 Neurons That Differ in Brain-wide Connectivity and Function. *Neuron* 88: 1253-67

Kim JS, Greene MJ, Zlateski A, Lee K, Richardson M, et al. 2014. Space-time wiring specificity supports direction selectivity in the retina. *Nature* 509: 331-36

647 Klein S, Staring M, Murphy K, Viergever MA, Pluim JP. 2010. elastix: a toolbox for intensity-based
648   medical image registration. *IEEE Trans Med Imaging* 29: 196-205
649 Krishnaswamy A, Yamagata M, Duan X, Hong YK, Sanes JR. 2015. Sidekick 2 directs formation of a
650   retinal circuit that detects differential motion. *Nature* 524: 466-70
651 Larkum M. 2013. A cellular mechanism for cortical associations: an organizing principle for the cerebral
652   cortex. *Trends Neurosci* 36: 141-51
653 Larkum ME, Petro LS, Sachdev RNS, Muckli L. 2018. A Perspective on Cortical Layering and Layer-
654   Spanning Neuronal Elements. *Front Neuroanat* 12: 56
655 LeCun Y, Bengio Y, Hinton G. 2015. Deep learning. *Nature* 521: 436-44
656 Lee WC, Bonin V, Reed M, Graham BJ, Hood G, et al. 2016. Anatomy and function of an excitatory
657   network in the visual cortex. *Nature* 532: 370-4
658 Lyamzin D, Benucci A. 2019. The mouse posterior parietal cortex: Anatomy and functions. *Neurosci Res*
659   140: 14-22
660 Niedworok CJ, Brown AP, Jorge Cardoso M, Osten P, Ourselin S, et al. 2016. aMAP is a validated
661   pipeline for registration and segmentation of high-resolution mouse brain data. *Nat Commun* 7:
662   11879
663 Osten P, Margrie TW. 2013. Mapping brain circuitry with a light microscope. *Nat Methods* 10: 515-23
664 Packer AM, McConnell DJ, Fino E, Yuste R. 2013. Axo-dendritic overlap and laminar projection can
665   explain interneuron connectivity to pyramidal cells. *Cereb Cortex* 23: 2790-802
666 Petreanu L, Mao T, Sternson SM, Svoboda K. 2009. The subcellular organization of neocortical excitatory
667   connections. *Nature* 457: 1142-5
668 Powell A, Connelly WM, Vasalauskaite A, Nelson AJD, Vann SD, et al. 2020. Stable Encoding of Visual
669   Cues in the Mouse Retrosplenial Cortex. *Cereb Cortex* 30: 4424-37
670 Ragan T, Kadiri LR, Venkataraju KU, Bahlmann K, Sutin J, et al. 2012. Serial two-photon tomography for
671   automated ex vivo mouse brain imaging. *Nat Methods* 9: 255-8
672 Rancz EA, Moya J, Drawitsch F, Brichta AM, Canals S, Margrie TW. 2015. Widespread vestibular
673   activation of the rodent cortex. *J Neurosci* 35: 5926-34
674 Reardon TR, Murray AJ, Turi GF, Wirblich C, Croce KR, et al. 2016. Rabies Virus CVS-N2c(DeltaG)
675   Strain Enhances Retrograde Synaptic Transfer and Neuronal Viability. *Neuron* 89: 711-24
676 Rees CL, Moradi K, Ascoli GA. 2017. Weighing the Evidence in Peters' Rule: Does Neuronal Morphology
677   Predict Connectivity? *Trends Neurosci* 40: 63-71
678 Richards BA, Lillicrap TP, Beaudoin P, Bengio Y, Bogacz R, et al. 2019. A deep learning framework for
679   neuroscience. *Nat Neurosci* 22: 1761-70
680 Rieubland S, Roth A, Hausser M. 2014. Structured connectivity in cerebellar inhibitory networks. *Neuron*
681   81: 913-29
682 Rockland KS, Pandya DN. 1979. Laminar origins and terminations of cortical connections of the occipital
683   lobe in the rhesus monkey. *Brain Res* 179: 3-20
684 Rogers A, Beier KT. 2021. Can transsynaptic viral strategies be used to reveal functional aspects of
685   neural circuitry? *J Neurosci Methods* 348: 109005
686 Romand S, Wang Y, Toledo-Rodriguez M, Markram H. 2011. Morphological development of thick-tufted
687   layer v pyramidal cells in the rat somatosensory cortex. *Front Neuroanat* 5: 5
688 Roth MM, Dahmen JC, Muir DR, Imhof F, Martini FJ, Hofer SB. 2016. Thalamic nuclei convey diverse
689   contextual information to layer 1 of visual cortex. *Nat Neurosci* 19: 299-307
690 Rothman JS, Silver RA. 2018. NeuroMatic: An Integrated Open-Source Software Toolkit for Acquisition,
691   Analysis and Simulation of Electrophysiological Data. *Front Neuroinform* 12: 14
692 Schaefer AT, Larkum ME, Sakmann B, Roth A. 2003. Coincidence Detection in Pyramidal Neurons Is
693   Tuned by Their Dendritic Branching Pattern. *Journal of Neurophysiology* 89: 3143-54
694 Schindelin J, Arganda-Carreras I, Frise E, Kaynig V, Longair M, et al. 2012. Fiji: an open-source platform
695   for biological-image analysis. *Nat Methods* 9: 676-82
696 Shipp S. 2016. Neural Elements for Predictive Coding. *Front Psychol* 7: 1792
697 Sun B, Lv B, Dong Q, Wang S, Chai Z. 2009. Watching moving images specifically promotes
698   development of medial area of secondary visual cortex in rat. *Dev Neurobiol* 69: 558-67
699 Takahashi N, Ebner C, Sigl-Glockner J, Moberg S, Nierwetberg S, Larkum ME. 2020. Active dendritic
700   currents gate descending cortical outputs in perception. *Nat Neurosci* 23: 1277-85
701 Takahashi N, Oertner TG, Hegemann P, Larkum ME. 2016. Active cortical dendrites modulate perception.
702   *Science* 354: 1587-90

703   Taube JS. 2007. The head direction signal: origins and sensory-motor integration. *Annu Rev Neurosci* 30:
704   181-207
705   Tyson AL, Rousseau CV, Niedworok CJ, Keshavarzi S, Tsitoura C, Margrie TW. 2020.
706   Velez-Fort M, Bracey EF, Keshavarzi S, Rousseau CV, Cossell L, et al. 2018. A Circuit for Integration of
707   Head- and Visual-Motion Signals in Layer 6 of Mouse Primary Visual Cortex. *Neuron* 98: 179-91
708   e6
709   Wang Q, Ding SL, Li Y, Royall J, Feng D, et al. 2020a. The Allen Mouse Brain Common Coordinate
710   Framework: A 3D Reference Atlas. *Cell* 181: 936-53 e20
711   Wang XJ, Pereira U, Rosa MG, Kennedy H. 2020b. Brain connectomes come of age. *Curr Opin*
712   *Neurobiol* 65: 152-61
713   Wickersham IR, Lyon DC, Barnard RJ, Mori T, Finke S, et al. 2007. Monosynaptic restriction of
714   transsynaptic tracing from single, genetically targeted neurons. *Neuron* 53: 639-47
715   Yamawaki N, Li X, Lambot L, Ren LY, Radulovic J, Shepherd GMG. 2019. Long-range inhibitory
716   intersection of a retrosplenial thalamocortical circuit by apical tuft-targeting CA1 neurons. *Nat*
717   *Neurosci* 22: 618-26
718   Young H, Belbut B, Baeta M, Petreanu L. 2021. Laminar-specific cortico-cortical loops in mouse visual
719   cortex. *Elife* 10
720   Zeng H. 2018. Mesoscale connectomics. *Curr Opin Neurobiol* 50: 154-62
721   Zhang S, Xu M, Kamigaki T, Hoang Do JP, Chang WC, et al. 2014. Selective attention. Long-range and
722   local circuits for top-down modulation of visual cortex processing. *Science* 345: 660-5

723

Supplementary material
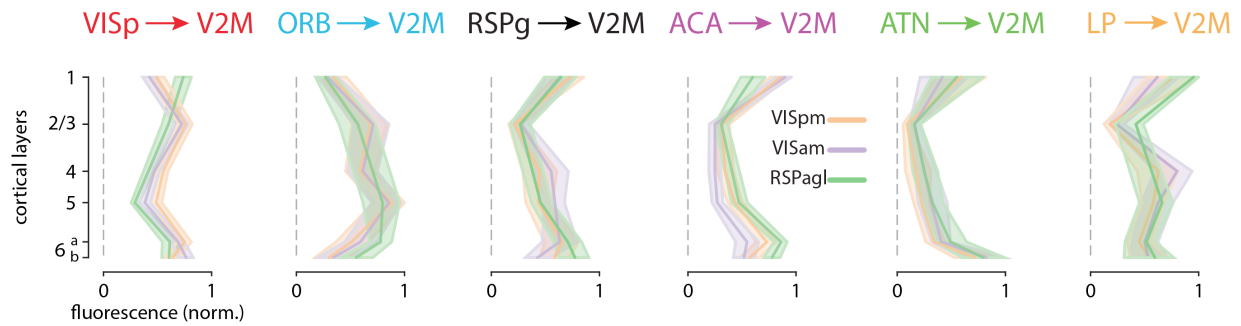
Figure S1. Comparison of axonal projection profiles. Layer-wise axonal projection profiles to VISpm, VISam and RSPagl. Data from the Allen Mouse Brain Connectivity Atlas.
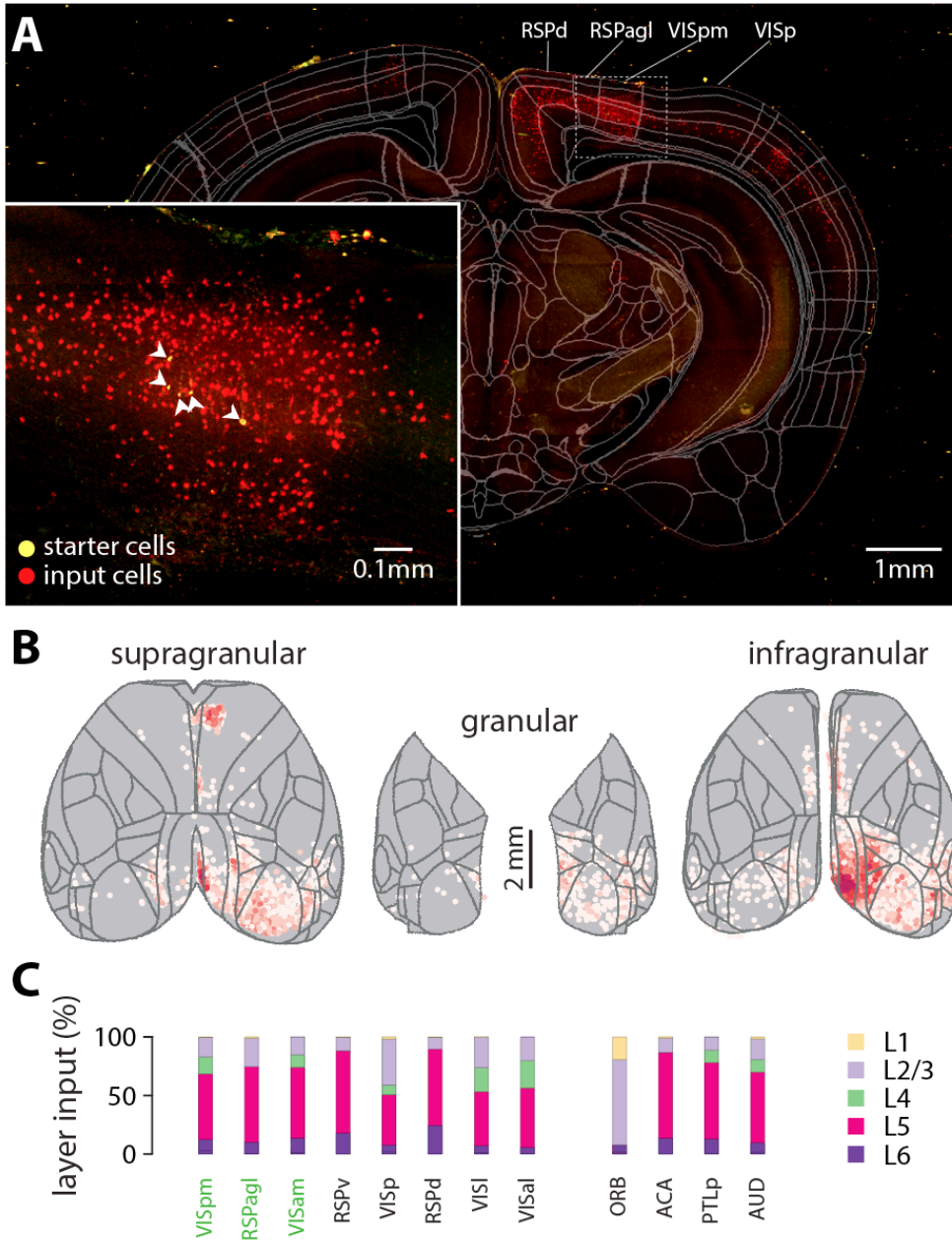
Figure S2. A. Maximum intensity projection of a 200 μm thick coronal slab containing some of the starter neurons. The propagated CCFv3 atlas outlines are overlayed. Inset shows starter area with higher magnification. **B.** Input cell density maps across supragranular, granular and infragranular layers. A-B Same experiment and scales as Figure 1. **C.** Distribution of input cells across cortical layers. Average of 3 experiments.
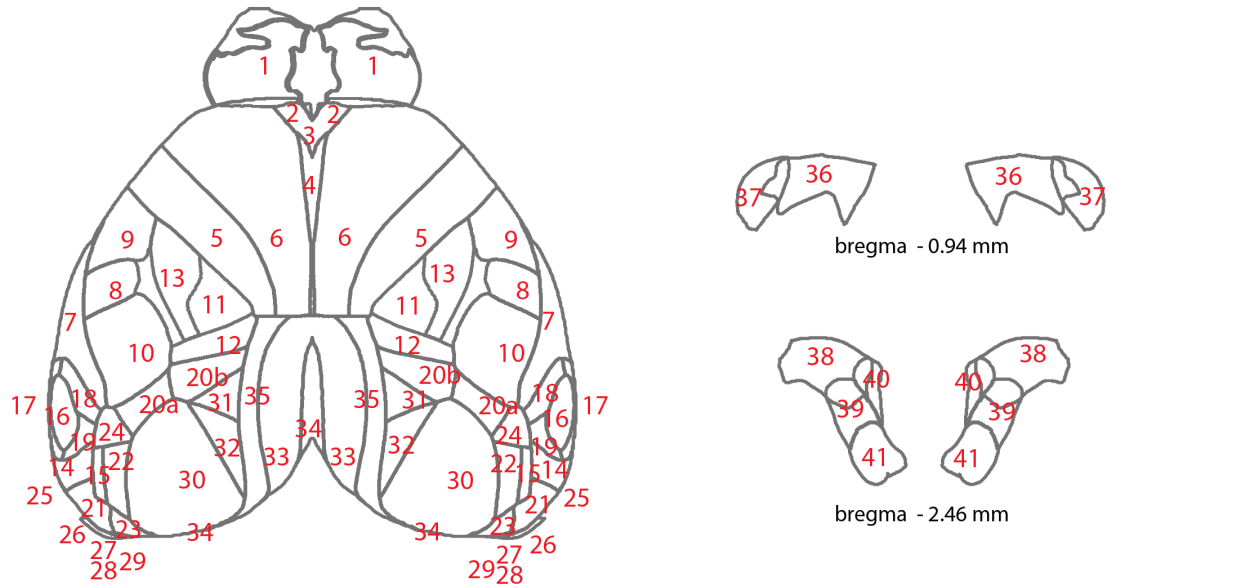
Cortex

1	Main olfactory bulb	MOB	20	Posterior parietal association areas	PTLp
2	Orbital area	ORB	20a	Rostrolateral visual area	VISrl
3	Prelimbic area	PL	20b	Anterior area	VISa
4	Anterior cingulate area	ACA	21	Postrhinal area	VISpor
5	Primary motor area	MOp	22	Lateral visual area	VISl
6	Secondary motor area	MOs	23	Posterolateral visual area	VISpl
7	Supplemental somatosensory area	SSs	24	Anterolateral visual area	VISal
8	Primary somatosensory area, nose	SSp-n	25	Ectorhinal area	ECT
9	Primary somatosensory area, mouth	SSp-m	26	Entorhinal area	ENT
10	Primary somatosensory area, barrel field	SSp-bfd	27	Presubiculum	PRE
11	Primary somatosensory area, lower limb	SSp-ll	28	Postsubiculum	POST
12	Primary somatosensory area, trunk	SSp-tr	29	Area prostriata	Apr
13	Primary somatosensory area, upper limb	SSp-ul	30	Primary visual area	VISp
14	Temporal association areas	TEa	31	Anteromedial visual area	VISam
15	Laterointermediate area	VISli	32	posteromedial visual area	VISpm
16	Primary auditory area	AUDp	33	Retrosplenial area, dorsal part	RSPd
17	Ventral auditory area	AUDv	34	Retrosplenial area, ventral part	RSPv
18	Dorsal auditory area	AUDd	35	Retrosplenial area, lateral agranular part	RSPagl
19	Posterior auditory area	AUDpo			

Thalamus

|						
36	Lateral posterior nucleus of the thalamus	LP	39	Anteroventral nucleus of thalamus	AV
37	Dorsal part of the lateral geniculate complex	LGd	40	Anterodorsal nucleus	AD
38	Lateral dorsal nucleus of thalamus	LD	41	Anteromedial nucleus	AM

736

737

738 **Figure S3.** Brain segmentation and nomenclature according to the Allen CCFv3.

739

Number of input cells

| thalamus	average	sd	sample 1	sample 2	sample 3						
LP	1191	191	1409	1052	1111						
ATN	1001	417	1465	657	882						
LGd	194	174	366	198	19	**Layerwise contribution**					
proximal cortex						**L1**	**L2/3**	**L4**	**L5**	**L6a**	**L6b**
VISp	1245	282	954	1262	1518	1.83%	39.36%	8.10%	42.97%	5.97%	1.77%
VISpm	842	264	687	692	1146	0.28%	16.63%	14.62%	55.98%	9.68%	2.80%
VISam	418	227	234	348	672	0.00%	15.12%	10.75%	60.37%	12.43%	1.32%
VISl	334	144	170	392	439	0.17%	25.97%	20.55%	46.06%	5.92%	1.33%
VISal	118	65	46	174	133	0.00%	20.08%	23.55%	50.62%	5.36%	0.40%
RSPv	1825	844	2705	1022	1747	0.29%	11.40%	n/a	70.43%	17.87%	0.01%
RSPd	1038	314	1256	678	1180	0.29%	9.97%	n/a	65.15%	24.45%	0.14%
RSPagl	785	353	967	378	1010	1.14%	24.25%	n/a	64.46%	9.96%	0.19%
distal cortex											
ORB	305	117	181	320	414	19.25%	72.86%	n/a	6.22%	1.67%	0.00%
ACA	252	161	189	131	435	0.96%	12.20%	n/a	73.28%	13.56%	0.00%
PTLp	221	87	120	266	276	0.00%	11.16%	10.62%	65.23%	12.60%	0.39%
AUD	177	28	145	195	192	1.58%	17.60%	10.83%	60.17%	8.18%	1.64%

740

741 **Supplementary table 1.** Results of rabies tracing experiments.

742
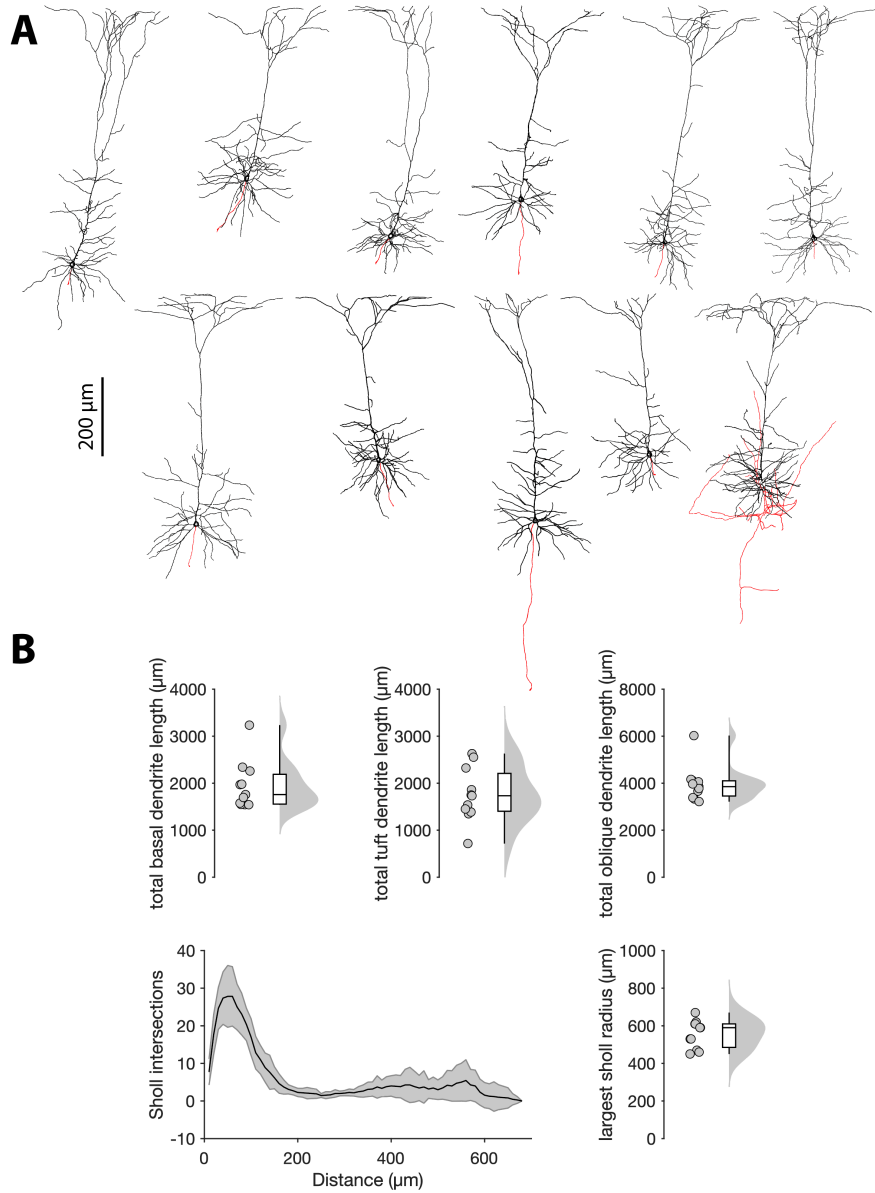
Figure S4. A. Reconstructed morphologies of 11 Colgalt-2 neurons. Black: dendrites; red: axons. **B.** Quantitative descriptive measures of dendritic morphology.

745
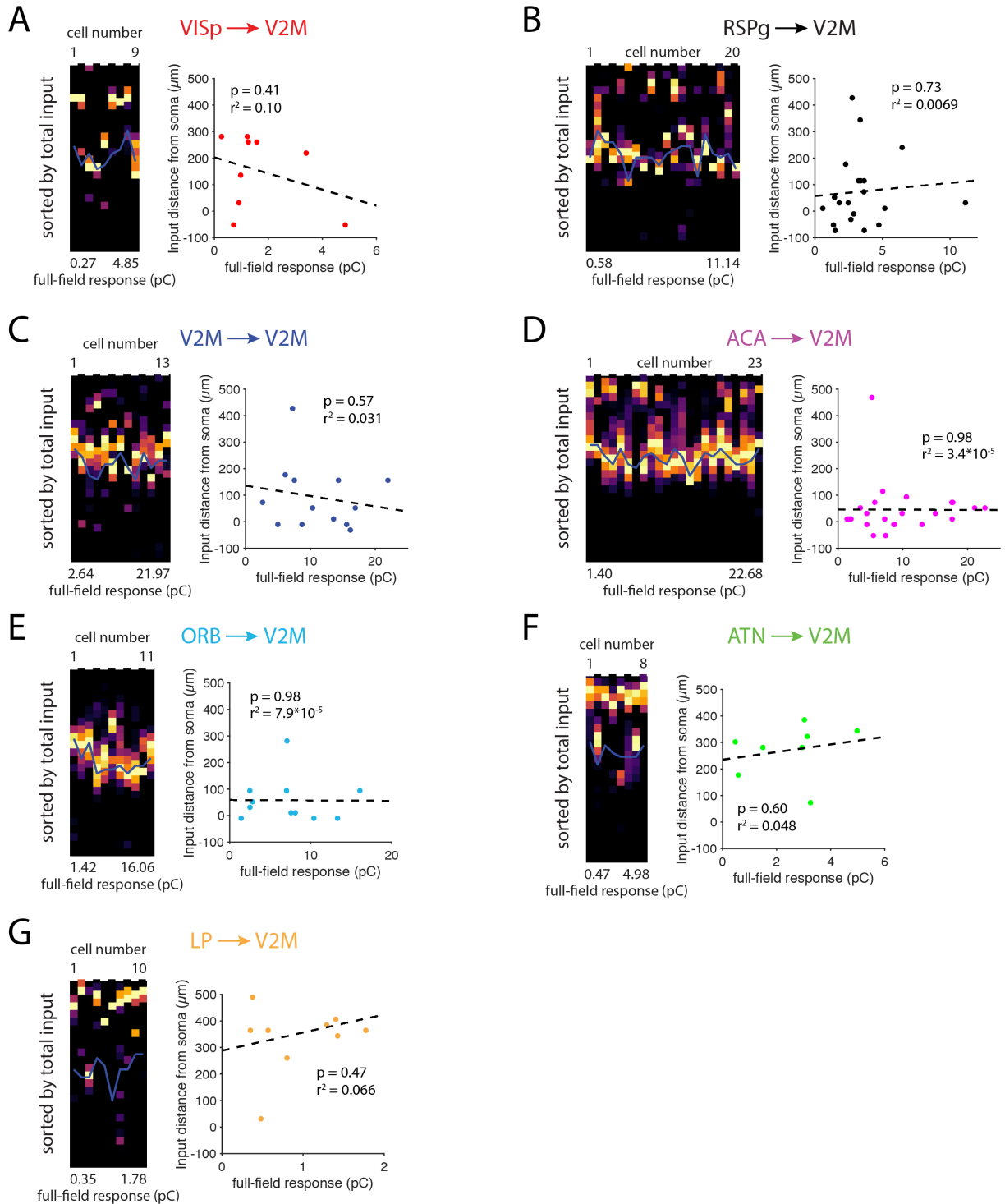
746
747
748 **Figure S5. Input location does not correlate with input strength. A.** Horizontal projections of VISp input to
749 individual cells sorted by full-field stimulation response. Right: Location of the largest input peak versus full-field
750 response. Dashed line is a linear fit. **B-G.** Same as in A, but for RSPg, V2M, ACA, ORB, ATN and LP input.

751

752

input area	parameter	basal	oblique	tuft*		
VISp	peak location (µm)	-62.5	104.17	187.5	total input (pC)	0.93
N = 6	input proportion (%)	26%	33%	42%	total input SEM	0.11
n = 9	proportional input (pC)	0.24	0.30	0.39	soma depth (µm)	507 ± 22
	horizontal bias (µm) **	62.5	41.67	-20.83	cells with peak in tuft	5/9
V2M	peak location (µm)	-41.67	83.33	166.67	total input (pC)	11.24
N = 4	input proportion (%)	24%	62%	14%	total input SEM	1.56
n = 13	proportional input (pC)	2.68	6.96	1.60	soma depth (µm)	498 ± 15
	horizontal bias (µm) **	20.83	20.83	-20.83	cells with peak in tuft	1/13
RSPg	peak location (µm)	-41.67	41.67	125	total input (pC)	3.40
N = 9	input proportion (%)	30%	40%	30%	total input SEM	0.51
n = 20	proportional input (pC)	1.04	1.36	1.01	soma depth (µm)	503 ± 15
	horizontal bias (µm) **	20.83	20.83	0	cells with peak in tuft	2/20
ACA	peak location (µm)	-41.67	41.67	83.33	total input (pC)	9.46
N = 5	input proportion (%)	30%	45%	25%	total input SEM	1.32
n = 23	proportional input (pC)	2.83	4.22	2.41	soma depth (µm)	464 ± 9
	horizontal bias (µm) **	0	0	-20.83	cells with peak in tuft	1/23
ORB	peak location (µm)	-41.67	20.83	N/A	total input (pC)	7.16
N = 3	input proportion (%)	35%	57%	9%	total input SEM	1.43
n = 11	proportional input (pC)	2.47	4.05	0.63	soma depth (µm)	521 ± 19
	horizontal bias (µm) **	0	20.83	0	cells with peak in tuft	0/11
ATN	peak location (µm)	-104.17	104.17	104.17	total input (pC)	2.48
N = 3	input proportion (%)	8%	17%	75%	total input SEM	0.54
n = 8	proportional input (pC)	0.21	0.42	1.86	soma depth (µm)	435 ± 15
	horizontal bias (µm) **	20.83	41.67	20.83	cells with peak in tuft	6/8
LP	peak location (µm)	-41.67	20.83	62.5	total input (pC)	0.97
N = 4	input proportion (%)	10%	15%	75%	total input SEM	0.16
n = 10	proportional input (pC)	0.10	0.14	0.72	soma depth (µm)	500 ± 23
	horizontal bias (µm) **	-41.67	-20.83	-83.33	cells with peak in tuft	9/10
	total proportional input	**27%**	**49%**	**24%**	**sum total input (pC)**	**35.65**

*tuft measurements from pia, basal and oblique from soma

** negative means lateral, positive medial

753

754   **Supplementary table 2.** Results of all sCRACM experiments.
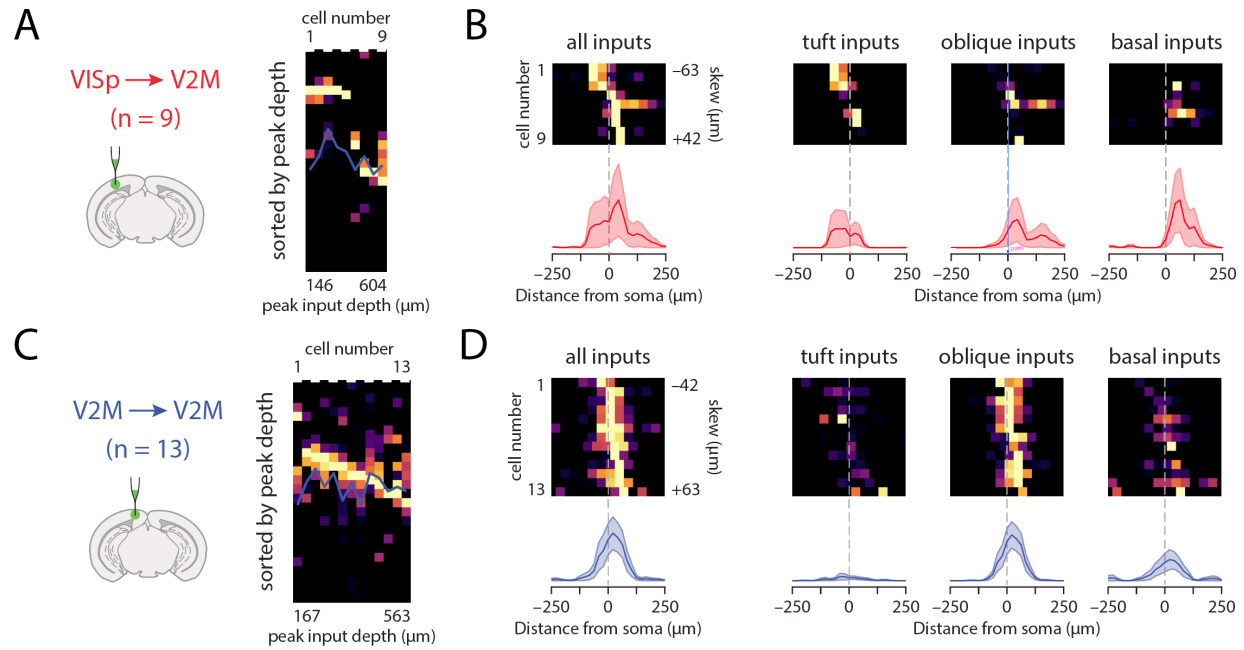
Figure S6. Detailed data analysis for VISp and V2M. A, C. Vertical projections of individual input maps sorted by the location of the peak input. **B, D.** Horizontal projections of individual input maps and their average for all inputs, and for domain-separated inputs.
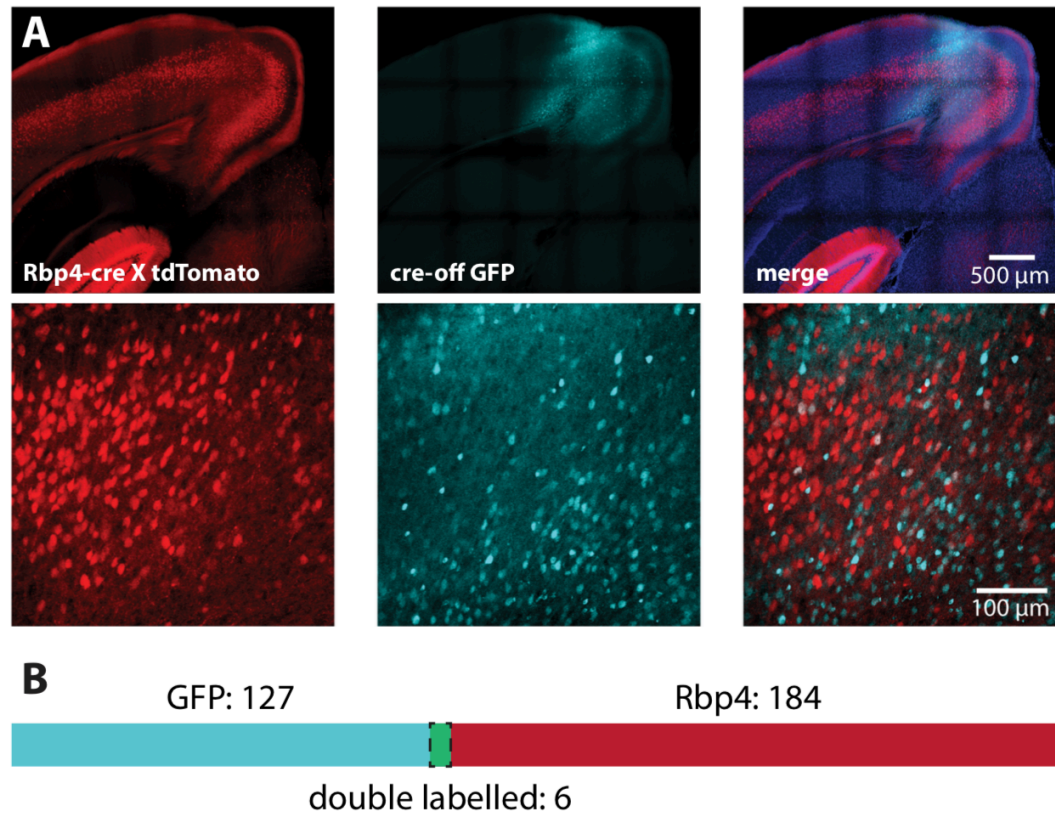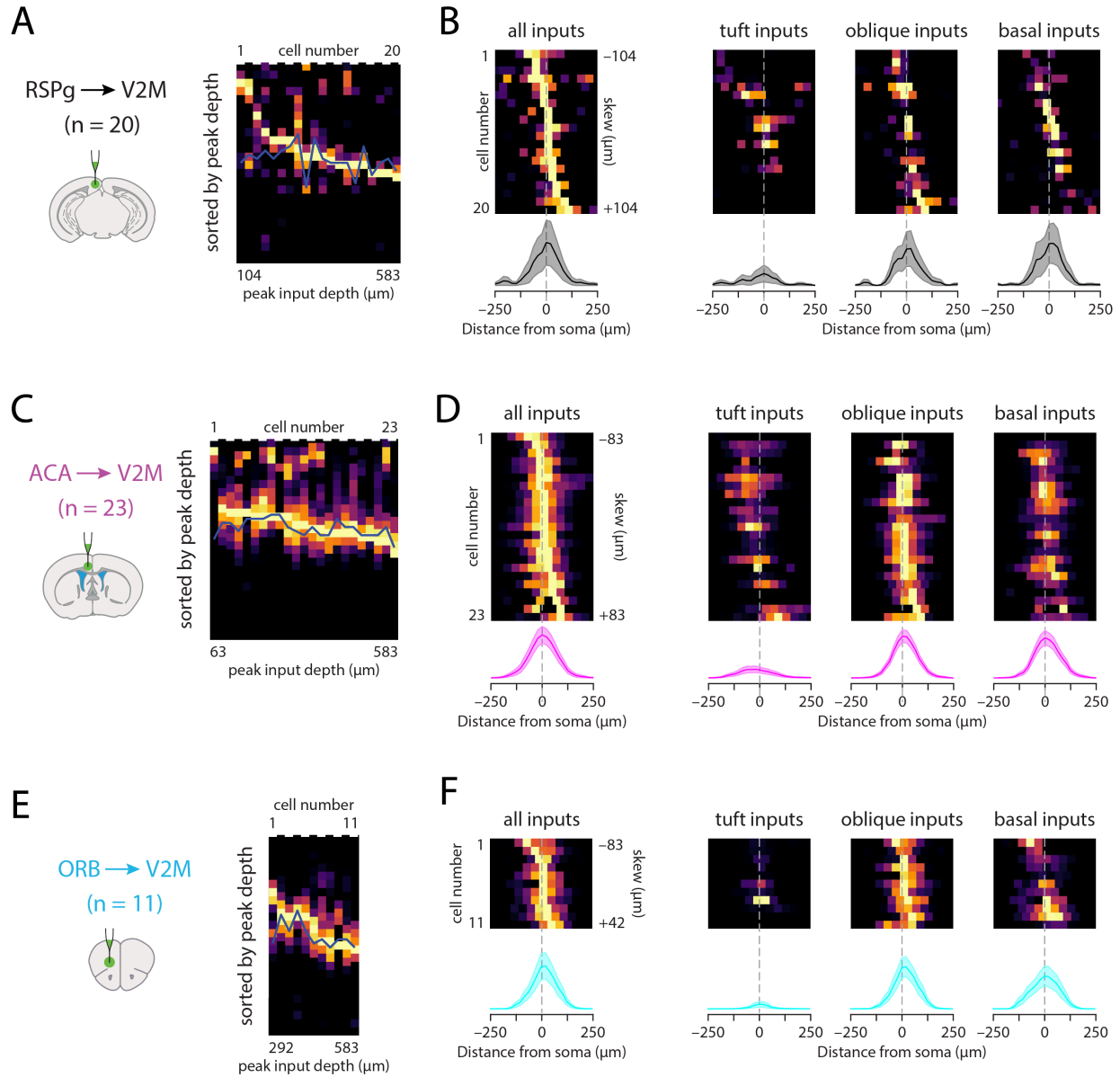
Figure S7. Efficacy of Cre-off virus. A. Example confocal images showing cre expression in L5 pyramidal neurons (red), GFP expression following cre-off virus injection (cyan) and overlap (blue = DAPI) on two magnifications. **B.** Quantification of overlap between cre and GFP expression.

763

Figure S8. Detailed data analysis for RSPg, ACA and ORB. A, C, E. Vertical projections of individual input maps sorted by the location of the peak input. **B, D, F.** Horizontal projections of individual input maps and their average for all inputs, and for domain-separated inputs.

767

768
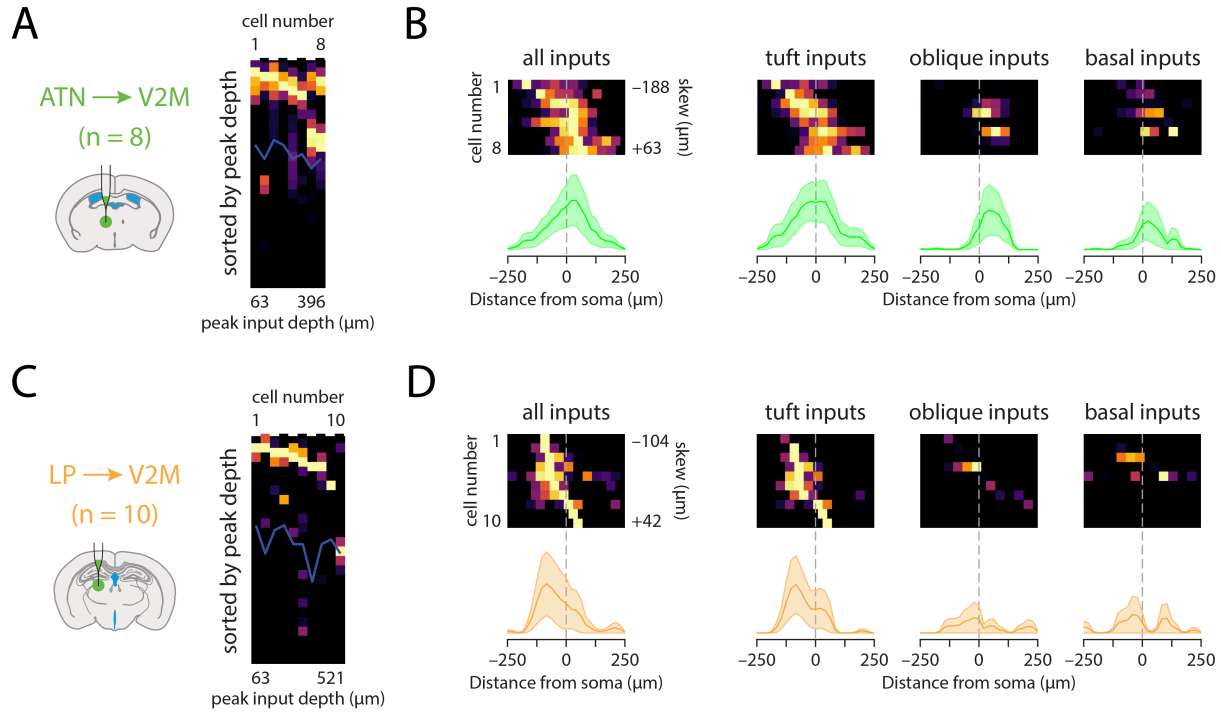
Figure S9. Detailed data analysis for ATN and LP. A, C. Vertical projections of individual input maps sorted by the location of the peak input. **B, D.** Horizontal projections of individual input maps and their average for all inputs, and for domain-separated inputs

772

Area	Distance from bregma (mm)	Mediolateral distance (mm)	Depth from pia (mm)	Number & volume of injections
VISp	[−3.5 : −2.8]	[1.8 : 2.7]	[0.5 : 0.6]	3 x 100 nL
RSPg	[−3.2 : −2.7]	0.5	[0.5 : 0.7]	2 x 100 nL
V2m	[−3.2 : −2.7]	1	[0.2 : 0.5]	2 x 100 nL
ACA	[0 : 1]	0.5	[1.2 : 1.5]	3 x 100 nL
ORB	[2 : 2.8]	1	[1.5 : 2.3]	3 x 100 nL
ATN	[−0.5 : −1.2]	[0.5 : 0.7]	[3.2 : 3.3]	2 x 100 nL
LP	[−2.5 : −1.7]	[1 : 1.5]	[2.4 : 2.6]	3 x 100 nL

773
774
775   **Supplementary table 3.** Stereotaxic coordinates and volumes of viral injections.